(2)

NONLINEAR DYNAMIC ANALYSIS OF EMBEDDED STRUCTURES

by

W.D. Liam Finn

EUROPEAN RESEARCH OFFICE OF THE U.S. ARMY

London, England

Contract Number: DAJA 45-86-C-0033

CORK GEOTECHNICS LTD.

March 7, 1988

Unclassified
SECURITY CLASSIFICATION OF THIS PAGE

REPORT DOCUMENTATION PAGE

Form Approved
OMB No 0704-0188
Exp Date: Jun 30, 1986

1a. REPORT SECURITY CLASSIFICATION Unclassified	1b. RESTRICTIVE MARKINGS --
2a. SECURITY CLASSIFICATION AUTHORITY	3. DISTRIBUTION/AVAILABILITY OF REPORT Approved for public release; distribution unlimited.
2b. DECLASSIFICATION/DOWNGRADING SCHEDULE	
4. PERFORMING ORGANIZATION REPORT NUMBER(S) 7 - 3 - 88	5. MONITORING ORGANIZATION REPORT NUMBER(S) R&D 5491-EN-01
6a. NAME OF PERFORMING ORGANIZATION Cork Geotechnic Ltd. 6b. OFFICE SYMBOL (If applicable)	7a. NAME OF MONITORING ORGANIZATION USARDSG-UK
6c. ADDRESS (City, State, and ZIP Code) 7 Heffernan Terrace Castlemartyr Co. Cork, Ireland	7b. ADDRESS (City, State, and ZIP Code) Box 65 FPO NY 09510-1500
8a. NAME OF FUNDING/SPONSORING ORGANIZATION USAE Waterways Experiment Station 8b. OFFICE SYMBOL (If applicable)	9. PROCUREMENT INSTRUMENT IDENTIFICATION NUMBER DAJA45-86-C-0033
8c. ADDRESS (City, State, and ZIP Code) PO Box 631 Vicksburg, MS 39180-0631	10. SOURCE OF FUNDING NUMBERS PROGRAM ELEMENT NO. 61102A; PROJECT NO. 1L161102BH57; TASK NO. 01; WORK UNIT ACCESSION NO

11. TITLE (Include Security Classification)

(U) Nonlinear Dynamic Analysis of Embedded Structures

12. PERSONAL AUTHOR(S)
W. D. Liam Finn

13a. TYPE OF REPORT	13b. TIME COVERED	14. DATE OF REPORT (Year, Month, Day)	15. PAGE COUNT
Final	FROM Jun 86 TO Aug 87	March 7, 1988	82

16. SUPPLEMENTARY NOTATION
--

17. COSATI CODES			18. SUBJECT TERMS (Continue on reverse if necessary and identify by block number)
FIELD	GROUP	SUB-GROUP	Nonlinear Dynamic Analysis, Hysteretic Stress-Strain Model, Seismic Centrifuge Tests, Seismic Porewater Pressures, Seismic Settlements, Accelerations, Displacements.
13	02		

19. ABSTRACT (Continue on reverse if necessary and identify by block number)

A computer program, TARA-3, developed at the University of British Columbia, Ireland for conducting nonlinear hysteretic dynamic response analysis is presented. The program can operate in either a total or effective stress mode. It may be used to analyse the seismic response of earth structures and soil-structure interaction systems such as nuclear containment structures. Validation studies of TARA-3 using data from seismic tests on centrifuged models are described. These studies confirm the capability of TARA-3 to predict accelerations, porewater pressures, and displacements in complex soil-structure systems during seismic loading with acceptable accuracy and reliability for engineering design.

Keywords: Earthquake Engineering,

20. DISTRIBUTION/AVAILABILITY OF ABSTRACT	21. ABSTRACT SECURITY CLASSIFICATION
☐ UNCLASSIFIED/UNLIMITED ☒ SAME AS RPT. ☐ DTIC USERS	Unclassified

22a. NAME OF RESPONSIBLE INDIVIDUAL	22b TELEPHONE (Include Area Code)	22c. OFFICE SYMBOL
Jerry C. Comati	441-402-7331	AMXSN-UK-RE

DD FORM 1473, 84 MAR 83 APR edition may be used until exhausted. All other editions are obsolete.

SECURITY CLASSIFICATION OF THIS PAGE
Unclassified

AD

NONLINEAR DYNAMIC ANALYSIS OF EMBEDDED STRUCTURES

by

W.D. Liam Finn

EUROPEAN RESEARCH OFFICE OF THE U.S. ARMY

London, England

Contract Number: DAJA 45-86-C-0033

CORK GEOTECHNICS LTD.

March 7, 1988

PREFACE

This report describes a method for nonlinear dynamic hysteretic response analysis of embankments and soil-structure interaction systems such as nuclear containment structures embedded in soil foundations under seismic loading. The analysis may be conducted in terms of total or effective stresses. The method is incorporated in the computer program TARA-3, developed at the University of British Columbia, Vancouver, Canada. Response parameters such as accelerations, stresses, porewater pressures, and dynamic and permanent deformations can be estimated using the program.

TARA-3 was validated using data from a series of simulated earthquake loading tests on centrifuged model structures which were conducted in the large geotechnical centrifuge at Cambridge University in the U.K. between 1983 and 1986. The earlier models were embankments or embankments carrying surface structures. Data from these models guided the evolution of TARA-3. Later centrifuge studies involved heavy structures embedded in both dry and saturated sand foundations which showed strong soil-structure interaction effects.

Data from the later studies are used to validate TARA-3 for conditions where there are very strong soil-structure interactions. Detailed comparisons of computed and measured responses of the test structures show that TARA-3 is capable of modelling dynamic soil-structure interaction with acceptable accuracy and reliability for engineering design.

The research was supported financially by the U.S. Nuclear Regulatory Commission through the European Research Office of the U.S. Army under Contract No. DAJA 45-86-C-0033 and by the National Science and Engineering Research Council of Canada under Grant No. 1498. The project was managed by W. Grabau and J.C. Comati of the European Research Office, U.S. Army, London, R.H. Ledbetter of U.S. Army Corps of Engineers (USAE), Waterways Experiment Station, Vicksburg, Miss. and L.L. Beratan, Office of Research, U.S. Nuclear Regulatory Commission. The centrifuge tests were conducted by R.S. Steedman of Cambridge University, U.K., under a separate contract. The tests were under the general direction of Professor A.N. Schofield, Cambridge University, and were monitored by R.H. Ledbetter and the author on behalf of USAE.

TABLE OF CONTENTS

NONLINEAR DYNAMIC ANALYSIS OF EMBEDDED STRUCTURES

INTRODUCTION

The basic elements in the dynamic analysis of a soil-structure system are input motion, appropriate models of site and structure, constitutive relations for all materials present, and a stable, efficient, accurate, computational procedure. The task of selecting representative input motions and an appropriately simplified model of the site depends heavily on what seismological, geological and geotechnical data are available and the judgment and experience of the engineer. The constitutive model and the procedure for analysis should be appropriate for the problem under consideration. The use of the simplest method of analysis that will provide reliable estimates of whatever response data is required is the best approach.

Linear elastic analysis is appropriate for low levels of shaking in relatively firm ground. As the shaking becomes more intense, soil response becomes nonlinear. A great variety of constitutive models are available for nonlinear response analysis ranging from equivalent linear elastic models to elastic-plastic models with both isotropic and kinematic hardening.

The most widely used methods for dynamic analysis are based on the equivalent linear model. Computer programs representative of this approach are SHAKE (Schnabel et al., 1972) for one-dimensional analysis (1-D) and FLUSH (Lysmer et al., 1975) for 2-D analysis. These programs perform total stress analyses and hence cannot take into account directly the effects of seismically induced porewater pressures on seismic response. Permanent deformations cannot be calculated directly either, since the methods are linear elastic. Equivalent linear models can exhibit pseudo-resonance, an amplification of computed response that is a function of the nature of the model only. This phenomenon can lead to increased design requirements (Finn et al., 1978).

The dynamic response characteristics and stability of an earth structure during earthquakes are controlled by the effective stress regime in the structure. In saturated regions of the structure, porewater pressures are induced by seismic excitation. These pressures continuously modify the effective stresses during the earthquake and hence have a major impact on dynamic response and stability; in extreme cases, they can trigger flow slides.

It is clearly a very important step in the design process to make reliable estimates of seismically induced porewater pressures. A semi-empirical method of estimation was developed by Seed (1979a), which is widely used in practice. Since 1976, there has been growing interest in the development and application of effective stress methods of dynamic response analysis (Finn et al., 1976, 1986; Dikmen and Ghabbousi, 1984; Ishihara and Towhata, 1982; Prevost et al., 1981; Siddharthan and Finn, 1982; Martin and Seed (1978); and Zienkiewicz et al., 1978). These methods model the important phenomenological aspects of dynamic response of saturated soils. However, because of a lack of data from suitably instrumented structures in the field it has not been possible to validate the quantitative predictive capabilities of the methods except in a few cases of level ground conditions (Finn et al., 1982; Iai et al, 1985).

A limited validation of some of these methods has been conducted using data from element tests such as cyclic triaxial or simple shear tests (Finn and Bhatia, 1980). Although this type of validation is an important first step, it is inadequate because in these tests either homogeneous stress or strain fields are prescribed. Therefore, the tests do not provide the rigorous trial of either the constitutive models or the robustness of the computational procedures that data from an instrumented structure in the field with inhomogeneous stress and strain fields would make possible.

Simulated earthquake testing of centrifuge models provides the most extensive data base for the detailed validation of methods of analysis. In a centrifuged model, stresses at the same levels that exist in a full scale structure at corresponding points can be produced by creating an artificial gravity field of intensity Ng, where g is the acceleration due to the gravity of the earth and 1/N is the linear scale of the model. This ability to create prototype stresses in the model is important since soil properties are dependent on effective stresses. Since the static stress levels in both model and prototype are similar at corresponding points, each soil element in the centrifuged model may be expected to undergo the same response history as corresponding elements in the prototype for a given excitation (Barton, 1982).

The United States Nuclear Regulatory Commission (USNRC) through the U.S. Army Corps of Engineers (USAE) sponsored a series of centrifuged model tests to provide data for the verification of the dynamic nonlinear effective

stress method of analysis incorporated in the program TARA-3 (Finn et al., 1986). The tests were conducted on the large geotechnical centrifuge at Cambridge University in the United Kingdom. Details of the Cambridge centrifuge and associated procedures for simulated earthquake testing have been described by Schofield (1981).

A previous report by Finn (1987) described validation studies on an earlier version of TARA-3 using data from the Cambridge centrifuge tests. The studies showed that TARA-3 was capable of reproducing all the phenomenological aspects of seismic response and gave reliable estimates of accelerations and porewater pressures. They also showed very clearly the capability of centrifuge modelling to provide extensive coherent data bases for validation of methods of analysis. Subsequent research on TARA-3 has resulted in improvements in the efficiency of some of the algorithms used in analysis, in the performance of slip elements which allow relative motion between structure and soil, and in the modelling of porewater pressure response, especially in calibrating the pore pressure model to either laboratory or field data. In addition, the capability of conducting consolidation analyses during the dynamic analysis has been added.

The current version of TARA-3 and validation studies of it are described in this report. Centrifuge model tests were run on a heavy two-dimensional structure embedded in both dry and saturated sand foundations. Previous 2-D centrifuge model tests involved embankments or embankments carrying surface structures. The additional complexities posed by the embedded structures provide a more rigorous test of the capability and reliability of TARA-3.

The program TARA-3 was used to predict accelerations, porewater pressures, and displacements in the centrifuge models and the results were compared with the measured responses. The studies confirm the reliability of TARA-3 in predicting the nonlinear dynamic effective stress response of soil structure systems under seismic loading.

METHOD OF STATIC ANALYSIS IN TARA-3

The program TARA-3 combines static and dynamic methods of analysis based on finite elements. Two types of elements are used, a 4-node isoparametric quadrilateral element with 8 degrees of freedom and a triangular element. The interpolation function that describes the variation of the displacement

within the finite element in terms of the nodal displacements ensures a linear variation of strain within the element.

Nonlinear static analysis is conducted using appropriately sized loading increments. The incremental equations, including porewater pressures, governing static response are

$$[K_t]\{\Delta\} = \{\Delta P\} - [K^*]\{\Delta U\} \qquad (1)$$

where $[K_t]$ is the global tangent stiffness matrix which depends on the tangent bulk and shear moduli as described later, $\{\Delta\}$ is the incremental nodal displacement vector, $\{\Delta P\}$ is the incremental nodal force vector, $[K^*]$ is the matrix associated with porewater pressures, and $\{\Delta U\}$ is the vector of incremental porewater pressures.

The in situ effective stress-strain regime in an earth structure prior to an earthquake is determined by an appropriate static analysis. In the case of constructed facilities, TARA-3 can model the construction sequence. During an earthquake, static analysis is also used to compute both the incremental changes in effective stresses resulting from incremental changes in porewater pressures and the continuing deformation of the soil structure under gravity forces.

The same constitutive laws are used in both static and dynamic analyses although different values of the moduli and strengths may be used in each analysis, if considered appropriate. The constitutive stress-strain model will be explained in the context of dynamic analysis only. The model for static analysis is derived by dropping those features applicable to dynamic analysis only.

Two important features of static analysis will be described here.

Failure Conditions

Failure is assumed to be governed by the Mohr-Coulomb failure criterion. The shear strength τ_{max} depends on the current stress state and the loading path. In nonlinear static analysis, it is widely assumed that the failure of a soil element is brought about by increasing the major principle effective stress, σ_1', while holding the minor principal effective stress, σ_3', constant (Duncan et al., 1978). This follows from conventional triaxial testing

conditions. Under this assumption, the maximum shear stress at failure in an element under the current stress state shown in Fig. 1, is given by

$$\tau_{max} = R \tag{2}$$

in which the radius, R, of the circle which touches the failure envelope (Fig. 2), is given by:

$$R = \frac{c' \cos \phi' + \sigma_3' \sin \phi'}{(1 - \sin \phi')} \tag{3}$$

Alternatively the maximum shear strength may be taken as the maximum shear stress on the failure plane given by

$$\tau_{max} = R \cos \phi' \tag{4}$$

In the field, the loading stresses may not follow the path of triaxial test conditions as assumed in the above derivation. For example, the soil mass may fail while the mean normal effective stress remains constant (Hardin and Drnevich, 1972). Under these conditions, in a plane strain problem, the centre of the Mohr circle remains fixed. The circle that represents failure can now be drawn by simply enlarging the initial Mohr circle until it touches the failure envelope (Fig. 3). In this case, the radius, R, of the failure circle is given by

$$R = c' \cos \phi' + \frac{(\sigma_x' + \sigma_y')}{2} \sin \phi' \tag{5}$$

As before there are two choices for τ_{max}

$$\tau_{max} = R \tag{6}$$

and

$$\tau_{max} = R \cos \phi' \tag{7}$$

These failure options are included in TARA-3 and one should invoke the option appropriate to the problem that is being analyzed.

Load Shedding During Local Failure

The stresses computed by incremental elastic analysis at any stage of loading or unloading must be checked continuously to ensure that they do not violate the failure criterion. A technique known as load shedding (Desai and Christian, 1979; Byrne and Janzen, 1984) is employed to redistribute excess stresses from elements which have failed to other elements in a sub-failure state. This technique has been applied successfully in the past for analysis of underground openings (Desai and Christian, 1979) and of tunnels and shafts (Byrne and Janzen, 1984). The deformations computed using the load shedding technique have been found to be in good agreement with closed form solutions (Byrne and Janzen, 1984).

Correction stresses are applied to each element having stress states that violate the failure criterion in order to restore stress compatibility (Fig. 4).

Let the stress state of the element which violates the Mohr-Coulomb failure criterion be given by $(\sigma'_x, \sigma'_y, \tau_{xy})$ and the correction stresses, $\{\Delta\sigma'\}$, by $(\Delta\sigma'_x, \Delta\sigma'_y, \Delta\tau_{xy})$.

During application of the correction stresses the mean normal stress is assumed to remain constant. Therefore the Mohr circles for the initial and corrected stress states are concentric.

It can be shown that

$$\Delta\sigma'_x = \left(\frac{\sigma'_x - \sigma'_y}{2}\right)\left(1 - \frac{R_c}{R_o}\right) \tag{8}$$

$$\Delta\sigma'_y = \left(\frac{\sigma'_y - \sigma'_x}{2}\right)\left(1 - \frac{R_c}{R_o}\right) \tag{9}$$

$$\Delta\tau_{xy} = \tau_{xy}\left(1 - \frac{R_c}{R_o}\right) \tag{10}$$

in which R_c is the radius of the corrected Mohr circle and R_o is the radius of the initial circle.

R_c and R_o are given by

$$R_c = c' \cos\phi' + \left(\frac{\sigma'_x - \sigma'_y}{2}\right) \sin\phi' \tag{11}$$

and

$$R_o = \left(\left(\frac{\sigma'_x - \sigma'_y}{2}\right)^2 + \tau_{xy}^2\right)^{1/2} \tag{12}$$

The correction stresses are converted to equivalent nodal forces, $\{\Delta f_{cor}\}$, (Byrne and Janzen, 1984), given by

$$\{\Delta f_{cor}\} = \iiint_V [B]^t \{\Delta\sigma'\}\, dV \tag{13}$$

in which $[B]^t$ is the transpose of the strain-displacement matrix [B]. The global nodal force vector, $\{\Delta F_{cor}\}$, is calculated taking the contribution from all the failed elements into account by

$$\{\Delta F_{cor}\} = \sum_{i=1}^{N_{fe}} \iiint_V [B]^t \{\Delta\sigma'\}\, dV \tag{14}$$

where N_{fe} is the total number of failed elements.

The incremental stresses, strains and deformations resulting from the application of the correction forces are added to the existing values.

METHOD OF DYNAMIC ANALYSIS IN TARA-3

An incrementally elastic approach using tangent shear and bulk moduli, G_t and B_t, respectively, has been adopted to model nonlinear behaviour. The incremental dynamic equilibrium forces $\{\Delta P\}$ are given by

$$[M]\{\ddot{\Delta x}\} + [C]\{\dot{\Delta x}\} + [K]\{\Delta x\} = \{\Delta P\} \tag{15}$$

where [M], [C] and [K] are the mass, damping and stiffness matrices respectively, and $\{\Delta x\}$, $\{\dot{\Delta x}\}$, $\{\ddot{\Delta x}\}$ are the matrices of incremental relative displacements, velocities and accelerations.

Mass Matrix

A lumped mass approximation to the mass matrix [M] is used instead of the more accurate consistent mass matrix. The presence of off-diagonal terms in the consistent mass matrix increases greatly the computational time

require to solve the dynamic equations of equilibrium. The lumped mass approximation is usually considered good enough for most geotechnical problems.

Stiffness Matrix

The stiffness matrix [K] is expressed in terms of the shear and bulk moduli and is formulated using the standard procedures of structural analysis (Zienkiewicz, 1977). Incremental stresses $\{\Delta\sigma\}$ and the incremental strains $\{\Delta\epsilon\}$ are related by the elasticity matrix [D] in the equation

$$\{\Delta\sigma\} = [D]\{\Delta\epsilon\} \tag{16}$$

where [D], for plane strain conditions, is given by

$$[D] = B_t \begin{bmatrix} 1 & 1 & 0 \\ 1 & 1 & 0 \\ 0 & 0 & 0 \end{bmatrix} + G_t \begin{bmatrix} 4/3 & -2/3 & 0 \\ -2/3 & 4/3 & 0 \\ 0 & 0 & 1 \end{bmatrix} \tag{17}$$

or

$$[D] = B_t[Q_1] + G_t[Q_2] \tag{18}$$

where $[Q_1]$ and $[Q_2]$ are constant matrices. This formulation reduces the computation time for reformulating [D] whenever G_t and B_t change in magnitude because of changes in shear strain or porewater pressure. The element stiffness matrix is given by

$$[k_t] = B_t \iiint_V [B]^t\,[Q_1][B]\,dV + G_t \iiint_V [B]^t\,[Q_2][B]\,dV \tag{19}$$

where [B] is the strain-displacement matrix (Zienkiewicz, 1977). The integral terms in this equation are constants and changes in the stiffness matrix due to changes in G_t and B_t are incorporated by simple multiplication.

Viscous Damping Matrix

The viscous damping is of the Rayleigh type and its use is optional. Very small amounts of viscous damping are used, typically equivalent to less than 1% of critical damping in the dominant response mode. Its primary

function is to control any high frequency oscillations that may arise from numerical integration in the vicinity of load reversal points. It also simulates the effect of flow of water throughout the soil structure. The element damping matrix is expressed as a linear combination of element mass matrix [m] and element tangent stiffness matrix $[k_t]$ as given in equation (20)

$$[c] = a[m] + b[k_t] \tag{20}$$

in which a and b are constants.

This formulation gives an equivalent critical damping ratio λ_n for the n^{th} mode

$$\lambda_n = \frac{a}{2\omega_n} + \frac{b\omega_n}{2} \tag{21}$$

where ω_n is the n^{th} mode frequency.

The element tangent stiffness matrix $[k_t]$ varies with time during the dynamic analysis. Therefore whenever $[k_t]$ is changed, the [c] matrix is also changed. TARA-3 has the option of maintaining [c] constant by expressing [c] in terms of the initial stiffness by

$$[c] = a[m] + b[k_t]_{t=0} \tag{22}$$

In TARA-3 the damping is primarily hysteretic and is automatically included as the hysteretic stress-strain loops are executed during analysis.

Correction Force Vector

The incremental equations of motion (15), are solved using the tangent stiffnesses at the beginning of each time increment. Therefore at the end of the time increment the computed strains and stresses for any element may not be compatible with the stress-strain relation of the soil. Correction forces are used to restore compatibility at the beginning of the next time increment. A condition of global equilibrium is satisfied on each application of correction forces.

Stress-Strain Behaviour in Shear

The behaviour of soil in shear is assumed to be nonlinear and hysteretic, exhibiting Masing behaviour (1926) during unloading and reloading.

The relationship between shear stress τ and shear strain γ for the initial loading phase under either drained or undrained loading conditions is assumed to be hyperbolic and given by

$$\tau = f(\gamma) = \frac{G_{max}\,\gamma}{(1 + (G_{max}/\tau_{max})\,|\gamma|)} \tag{23}$$

in which G_{max} is the maximum shear modulus and τ_{max} is the appropriate shear strength. This initial loading or skeleton curve is shown in Fig. 5(a). The unloading-reloading curves are modelled using the Masing criterion. This implies that the equation for the unloading curve from a point (γ_r,τ_r) at which the loading reverses direction, is given by

$$\frac{\tau-\tau_r}{2} = \frac{G_{max}(\gamma-\gamma_r)/2}{1 + (G_{max}/2\tau_{max})\,|\gamma-\gamma_r|} \tag{24}$$

or

$$\frac{\tau-\tau_r}{2} = f(\frac{\gamma-\gamma_r}{2}) \tag{25}$$

The shape of the unloading-reloading curve is shown in Fig. 5(b).

Finn et al. (1976) proposed rules for extending the Masing concept to irregular loading. They suggested that unloading and reloading curves follow the skeleton loading curve when the magnitude of the previous maximum shear strain is exceeded (Fig. 5c). When the current loading curve intersects the previous loading curve, the stress-strain curve follows the previous loading curve (Fig. 5d).

The tangent shear modulus, G_t, for a point on the skeleton curve is given by

$$G_t = \frac{G_{max}}{(1 + \frac{G_{max}|\gamma|}{\tau_{max}})^2} \tag{26}$$

At a stress point on an unloading or reloading curve G_t is given by

$$G_t = \frac{G_{max}}{\left(1 + \frac{G_{max}}{2\tau_{max}} |\gamma - \gamma_r|\right)^2} \tag{27}$$

Stress-Strain Behaviour in Hydrostatic Compression

The response of the soil to uniform all round pressure is assumed to be nonlinearly elastic and dependent on the mean normal stress. Hysteretic behaviour, if any, is neglected in this mode. The relationship between tangent bulk modulus, B_t, and mean normal effective stress, σ'_m, is assumed to be in the form

$$B_t = K_b P_a \left(\frac{\sigma'_m}{P_a}\right)^n \tag{28}$$

in which K_b is the bulk modulus constant, P_a is the atmospheric pressure in units consistent with σ'_m, and n is the bulk modulus exponent.

Effect of Porewater Pressures

As porewater pressures increase in saturated soils during seismic shaking the effective stresses decrease. The effective stress system is continually updated by solving the equilibrium equations (1) with $\{\Delta P\} = \{0\}$.

$$\{0\} = [K_t]\{\Delta\} + [K^*]\{\Delta U\} \tag{29}$$

The incremental displacements, strains and stresses given by this procedure constitute the response of the deposit to softening of the elements. The incremental strains are accumulated and they contribute to the permanent deformations of the soil structure. The incremental stresses give rise to the new effective stress system which can now be used to establish the current effective stress dependent soil properties. Both G_t and B_t depend on the current mean-normal effective stress. Therefore, as the porewater pressures increase and reduce the mean effective stresses, these parameters must be adjusted to be compatible with the updated effective stress system. For example, it is commonly assumed that $G_{max} \alpha (\sigma'_m)^{1/2}$, therefore

$$\frac{G}{G_{max}} = \left(\frac{\sigma'_m}{\sigma_{mo}}\right)^{1/2} \quad (30)$$

where G is the maximum shear modulus for the current cycle of loading.

If significant volumetric compaction occurs during seismic loading, the moduli should also be modified to reflect this strain hardening, following procedures outlined by Finn et al. (1976). The program continuously modifies the soil properties for the effects of both porewater pressures and dynamic strains.

RESIDUAL POREWATER PRESSURE MODEL

During seismic shaking two kinds of porewater pressures are generated in saturated sands; transient and residual. The transient pressures are due to changes in the applied mean normal stresses during seismic excitation. For saturated sands, the transient changes in porewater pressures are equal to changes in the mean normal stresses. Since they balance each other, the effective stress regime in the sand remains largely unchanged and so the stability and deformability of the sand is not seriously affected. Therefore these pressures are not modelled in TARA-3.

The residual porewater pressures are due to plastic deformations in the sand skeleton. These persist until dissipated by drainage or diffusion and therefore they exert a major influence on the strength and stiffness of the sand skeleton. Since both the shear and bulk moduli are dependent on the effective stresses in the soil, excess porewater pressures must be continually updated during analysis. The residual porewater pressures are modelled in TARA-3 using the model developed by Martin, Finn and Seed (1975). Therefore computed porewater pressure records will show the steady accumulation of residual porewater pressure with time but will not show the fluctuations in pressure caused by the transient changes in mean normal stresses.

In the Martin-Finn-Seed model the increments in porewater pressure ΔU that develop in a saturated sand under seismic shear strains are related to the volumetric strain increments $\Delta\epsilon_{vd}$ that occur in the same sand under drained conditions with the same shear strain history. This model applies

only to level ground so that there are no static shear stresses acting on horizontal planes prior to the earthquake. The M-F-S model is subsequently modified to include the effects of the initial static shear stresses present in 2-D analyses as described later.

The porewater pressure model is described by

$$\Delta U = \bar{E}_r \cdot \Delta\epsilon_{vd} \tag{31}$$

in which $\bar{E}_r$ is the one-dimensional rebound modulus of sand at an effective stress σ'_v.

Under drained simple shear conditions, the volumetric strain increment $\Delta\epsilon_{vd}$ is a function of the total accumulated volumetric strain ϵ_{vd} and the amplitude of the current shear strain γ, and is given by

$$\Delta\epsilon_{vd} = C_1(\gamma - C_2\epsilon_{vd}) + \frac{C_3\epsilon_{vd}^2}{\gamma + C_4\epsilon_{vd}} \tag{32}$$

in which C_1, C_2, C_3 and C_4 are volume change constants that depend on the sand type and relative density and may be determined directly by means of drained cyclic simple shear tests on dry or saturated samples. In practice simpler procedures are used as discussed in the next section.

An analytical expression for the rebound modulus $\bar{E}_r$, at any effective stress level σ'_v, is given by Martin et al. (1975) as

$$\bar{E}_r = \frac{d\sigma'_v}{d\epsilon_{vr}} = (\sigma'_v)^{1-m}/[m\, K_2(\sigma'_{vo})^{n-m}] \tag{33}$$

in which σ'_{vo} is the initial value of the effective stress and K_2, m and n are experimental constants derived from rebound tests in a consolidation ring.

Extension of M-F-S Model to 2-D Conditions

In the 2-D analysis of isotropic soil, the permanent volume changes due to shearing action are related to the cyclic shear stresses on horizontal planes because the seismic input motions are usually assumed to be shear waves propagating vertically. Therefore, in TARA-3, for computation of $\Delta\epsilon_{vd}$ in equation (32), the shear strain on the horizontal plane, γ_{xy}, is substituted in place of γ. Also, σ'_v and σ'_{vo} in equation (33) are replaced by σ'_y and

σ'_{yo} respectively, where σ'_y and σ'_{yo} are the current and initial vertical effective stresses.

Static shear stresses are usually present on the horizontal planes in 2-D problems. The presence of initial static shear stresses may significantly affect the cyclic behaviour of sands depending on the relative density of the sand and the level of the initial static shear stress (Seed and Lee, 1966; Vaid and Finn, 1978; Vaid and Chern, 1981). In saturated sands, the rate of development of porewater pressure, the level to which it may rise and the liquefaction potential curve are all dependent on the static shear stress level. These effects are taken into account in the porewater pressure model by specifying model constants such that they produce a reasonable match for the liquefaction potential curves and the rates of porewater pressure generation observed in laboratory samples with different initial static shear stress ratios.

Determination of Porewater Pressure Constants in Practice

The direct measurement of the constants in the porewater pressure model requires cyclic simple shear equipment which is not yet in common use. Therefore, to facilitate the use of TARA-3 in practice, techniques have been developed to derive the constants from the liquefaction resistance curve of the soil. The liquefaction curve may be determined from cyclic triaxial tests and then corrected to simple shear conditions as described by Seed (1979b) or derived directly from Standard Penetration Test data (Seed et al., 1983). In the latter case the constants are derived by a regression process to ensure that the predicted liquefaction curve compares satisfactorily with the field liquefaction curve using the program SIMCYC (Yogendrakumar and Finn, 1986a). If the liquefaction curve has been derived by laboratory tests, the rate of porewater pressure increase is known. Then a regression analysis is used to select constants that match both the rate of porewater pressure generation and the liquefaction curve using the program C-PRO (Yogendrakumar and Finn, 1986b).

Maximum Residual Porewater Pressure Criterion

Laboratory investigations of samples with initial static shear stress on potential failure planes (Chern, 1981) reveal that there is a limit to which the residual porewater pressures can rise. For triaxial conditions, the

limiting residual porewater pressure, U_{max}, has been found to be given by (Chern, 1981; Chang, 1982)

$$U_{max} = \sigma'_{3c} \left[1 - \left(\frac{\sigma'_{1c}}{\sigma'_{3c}} - 1\right) \frac{1 - \sin \phi'}{2 \sin \phi'}\right] \tag{34}$$

in which σ'_{1c} and σ'_{3c} are the major and minor principal consolidation stresses respectively and ϕ' is the angle of internal friction.

Equation (34) implies that the limiting value of the residual porewater pressure depends on the static shear stress level after the end of consolidation.

Loading from earthquakes resembles simple shear conditions more than triaxial conditions. Therefore, equation (34) has been modified to reflect this, giving

$$U_{max} = \sigma'_{3*} \left[1 - \left(\frac{\sigma'_{1*}}{\sigma'_{3*}} - 1\right) \frac{1 - \sin \phi'}{2 \sin \phi'}\right] \tag{35}$$

in which σ'_{1*} and σ'_{3*} are the applied major and minor principal stresses in a triaxial sample that produce stress conditions on a plane inclined at an angle $(45 + \phi'/2)$ to the horizontal which are the same as the initial stresses (σ'_y, τ_{xy}) on horizontal planes in the field (Fig. 6). Using the Mohr circle in Fig. 7, σ'_{1*} and σ'_{3*} can be calculated as,

$$\sigma'_{1*} = \sigma'_y + \tau_{xy} \frac{(1 + \sin \phi')}{\cos \phi'} \tag{36}$$

$$\sigma'_{3*} = \sigma'_y - \tau_{xy} \frac{(1 - \sin \phi')}{\cos \phi'} \tag{37}$$

Note that equation (35) gives the initial vertical stress as the limit on peak residual porewater pressure for the case of level ground. TARA-3 also includes the option of limiting the porewater pressure increase to that reached when failure occurs according to the Mohr-Coulomb criterion.

Special Features of the Analysis

Dynamic analyses are conducted in current engineering practice without including the effects of gravity or previous strains. However, as strength

and stiffness degrade during seismic excitation because of increasing porewater pressures, the structure deforms under the gravitational forces. This effect is taken into account in TARA-3.

In current practice, static analyses are usually conducted only to determine the initial static stress conditions so that appropriate initial moduli may be selected. Dynamic analysis is started from a zero strain condition. TARA-3 also has the capability to begin from zero strain or from the initial state of strain due to static loading. The latter procedure leads to the best modelling of plastic deformations.

For analysis involving soil-structure interaction, it is important to model slippage between the structure and soil. Slip may occur during very strong shaking or even under moderate shaking if high porewater pressures are developed under the structure. TARA-3 contains slip elements of the Goodman type (1968) to allow for relative movement between soil and structure in both sliding and rocking modes of response during earthquake excitation.

TARA-3 incorporates an energy transmitting base and lateral energy transmitting boundaries.

The three components of permanent deformation in a soil structure system as a result of earthquake loading are computed by TARA-3. The first component is the dynamic residual deformation that occurs as a result of the hysteretic stress-strain response. The second component is the deformation under gravity loading when increasing porewater pressures during the earthquake reduce the stiffness of the dam. The third component is the deformation of the system that occurs due to consolidation as the seismically induced residual porewater pressures dissipate. The post earthquake deformation field is the sum of all three deformation components.

SOIL PROPERTIES FOR TARA-3 ANALYSES

The centrifuge model tests used in the verification of TARA-3 were conducted over a three year period from 1983 to 1986. In 1983 the technology for conducting seismic tests on large scale models was in its infancy and techniques were not available for measuring the in-situ properties of the sand models in flight. Not until 1987 (Finn and Gohl, 1987) was a technique developed for measuring reliably the in-situ shear modulus. This technique

involves measuring shear wave velocities using piezoceramic bender elements in the sand model while the model is in flight.

Therefore, the soil properties required for the TARA-3 analyses had to be derived using other procedures. It is fortunate that the constitutive model in TARA-3 is based on three robust parameters, shear modulus, bulk modulus and shear strength which can be related to the relative density and effective stresses in the model. Hence the required soil properties were estimated on the basis of the relative density of the model.

The gross density of a model was determined from its geometry and weight. The relative density was then calculated from a knowledge of the density at minimum and maximum void ratios of the sand.

Model Parameters for Shearing Deformation

The maximum shear modulus, G_{max}, and the maximum shear strength, τ_{max}, may be specified directly by the user using field or laboratory measurements or may be computed in the program TARA-3 from given soil data. The most reliable values of G_{max} may be obtained from shear wave velocity measurements in the field.

The initial in-situ shear modulus may also be calculated using the equation proposed by Seed and Idriss (1970)

$$G_{max} = 1000\ K_{2max}(\sigma'_m)^{1/2}\ (OCR)^k \qquad \text{(in psf)} \qquad (38)$$

in which K_{2max} is a constant which depends on the type of sand and the relative density, OCR is the overconsolidation ratio, and k is a constant dependent on plasticity. An equivalent nondimensional form is

$$G_{max} = 21.7\ K_{2max}P_a(OCR)^k\ \left(\frac{\sigma'_m}{P_a}\right)^{1/2} \qquad (39)$$

in which P_a is the atmospheric pressure in the same units as σ'_m.

Values of the shear modulus parameter, K_{2max} are given by Seed and Idriss (1970) for various relative densities (Fig. 8). They may also be obtained using an expression proposed by Byrne (1981) as shown in equation (40)

$$K_{2max} = 15 + 0.61\ D_r \tag{40}$$

in which D_r is the relative density expressed as a percentage.

G_{max} may also be determined using the equation proposed by Hardin and Drnevich (1972) which is structurally similar to equation (39).

$$G_{max} = 320.8\ P_a \frac{(2.973 - e)^2}{(1 + e)} (OCR)^k \left(\frac{\sigma'_m}{P_a}\right)^{1/2} \tag{41}$$

in which e is the void ratio.

Finn and Gohl (1987) showed that the correlations proposed by Seed and Idriss (1970) and Hardin and Drnevich (1972) give very good estimates of shear moduli for centrifuge models in flight by comparing estimates by these procedures with moduli measured directly in situ using their new technique.

Although no clays were incorporated in the model foundations, information of clay moduli are presented to complete the properties list for TARA-3. For clays, the maximum shear modulus is estimated from the undrained shear strength, S_u, using the equation

$$G_{max} = K_{clay}\ S_u \tag{42}$$

in which K_{clay} is a constant for a given clay.

The variation of G/S_u with shear strain for saturated clays is shown in Fig. 9 (Seed and Idriss, 1970). Typical values of K_{clay} range from 1000 to 3000.

Bulk Modulus Parameters

The bulk modulus parameters, K_b and n, in equation (28), can be determined using conventional triaxial test data, following procedures proposed by Duncan et al. (1978, 1980). They can also be obtained from isotropic consolidation tests as described by Byrne (1981).

Typical values of K_b vary between 300 and 1000 depending on the relative density of the soil and soil type. Tables of K_b and n applicable to many sands are presented by Byrne (1981) and Byrne and Cheung (1984).

The bulk modulus parameter, K_b, for static analysis was obtained using the expression reported by Byrne and Cheung (1984). This takes the form

$$K_b = \frac{19}{0.0655 - 0.0535 \log \frac{D_r}{10}} \quad (43)$$

where D_r is the relative density expressed in percentage.

For saturated undrained conditions values of K_b much larger than that given by equation (43) are used to simulate the constant volume condition usually assumed in undrained analysis. The bulk modulus exponent, n, was selected to be equal to 0.40.

The effective angle of internal friction, ϕ', of the Leighton Buzzard sand was determined by both triaxial tests (Eyton 1982) and simple shear tests and over the range of density used in the model tests was taken to be around 35 degrees.

Liquefaction Resistance Curve

The liquefaction resistance of the Leighton Buzzard sand was determined using the University of British Columbia simple shear device (Finn et al., 1971). The liquefaction resistance was determined for a relative density of D_r = 65% and is shown in Fig. 10. Resistance at other relative densities within the range of the test data were estimated on the assumption of a linear dependence on relative density (Seed and Lee, 1966).

The volume change constants C_1 to C_4 and the rebound constants in the Martin-Finn-Seed porewater pressure model were determined by regression analysis using SIMCYC (Yogendrakumar and Finn, 1986a) to result in a close fit between the measured and predicted liquefaction resistance curves. Table 1 gives the set of volume change and rebound constants for different relative densities used in the tests.

Table 1 Porewater Pressure Model Constants

Constants	D_r = 64%	D_r = 52%
C_1	0.960	1.00
C_2	0.430	0.40
C_3	0.161	0.161
C_4	0.376	0.376
m	0.430	0.430
n	0.620	0.620
K_r	0.008	0.007

Structural Properties

The structural response is assumed to be linearly elastic in the analyses and therefore the structure was modelled using linear elastic elements.

The properties selected for aluminum alloy (Dural) are shown in Table 2.

Table 2 Structural Properties

Property	Aluminum
Specific Gravity	2.83
Unit Weight (kN/m^3)	27.8
Shear Modulus (kPa)	2.4×10^7
Bulk Modulus (kPa)	6.7×10^7
Poisson Ratio	0.30
Damping Coefficient, α	0.0
Damping Coefficient, β	0.005

Slip Element Properties

Experimental studies by many researchers (Tatsuoka et al., 1985; Uesugi et al., 1986) on the behaviour of sand-structure interfaces under cyclic loading reveal that the interface behaviour is essentially of the rigid-perfectly plastic type. Typical properties for a slip element are tabulated in Table 3.

Table 3 Slip Element Properties

Property	Slip Element
Unit Normal Stiffness (kPa/m)	6.3×10^5
Unit Shear Stiffness (kPa/m)	6.3×10^5
Friction Angle, ϕ'_s	10.0
Cohesion, c_s	0.0

SEISMIC TESTS ON CENTRIFUGED MODELS

A series of seismic tests on centrifuged models was conducted in the Cambridge University Geotechnical Centrifuge to obtain data on the seismic response of foundation soils carrying both surface and embedded structures. The data were used in validating TARA-3. The tests were sponsored by the Nuclear Regulatory Commission (NRC) through the U.S. Army Corps of Engineers (USAE). Full details of the centrifuge tests discussed in this report are described in a Cambridge University report by Steedman (1986).

Details of the Cambridge geotechnical centrifuge and associated procedures for simulated earthquake testing have been described by Schofield (1981). Seismic excitation of centrifuged models in the Cambridge centrifuge is generated by a wheel attached to the model container travelling on a track with precisely machined undulations attached to the wall of the centrifuge pit and extending over one-third of the circumference. The system is referred to as the Bumpy Road. The intensity of model shaking is controlled by adjusting the linkage between wheel and model container. For a given Bumpy Road configuration, frequency of oscillation is governed by the angular velocity of the rotor arm of the centrifuge.

Ideally, the Bumpy Road should generate sinusoidal pulses but resonances, mechanical linkage clearances and other factors result in some high frequency signals which broaden the frequency input range. In particular, the model earthquake consists of three distinct phases:

(1) small "wheel-on" accelerations associated with initial contact of the wheel with the track;

(2) the model earthquake proper consisting of roughly sinusoidal pulses;

(3) small "wheel-off" accelerations associated with the wheel leaving the track.

The base input motion is transmitted through the model primarily by shear stresses but also by normal stresses due to bending modes. However, some high frequency acceleration spikes are introduced due to the effects of the sides of the container and container resonances.

De-aired silicon oil was used as a pore fluid in saturated models in order to model the drainage conditions in the prototype during the earthquake. If the linear scale factor between model and prototype is N, then excess porewater pressures dissipate approximately N^2 times faster in the

model than in the prototype if the same fluid is used in both. The rate of loading by seismic excitation will be only N times faster. Therefore, to model prototype drainage conditions during the earthquake, a pore fluid with a viscosity N times the prototype viscosity must be used. This viscosity was achieved by an appropriate blending of commercial silicon oils. Tests by Eyton (1982) have shown that the stress-strain behaviour of fine sand is not changed when silicon oil is substituted for water as a pore fluid.

Model Test Structure

A schematic view of the structure used in the centrifuge tests is shown in Fig. 11. This configuration with strong soil-structure interaction provides a very severe test of the capabilities of TARA-3 to model dynamic response. The structure is made from a solid piece of aluminum alloy and has dimensions 150mm wide by 108mm high in the plane of shaking. The length perpendicular to the plane of shaking is 470mm and spans the width of the model container. The structure is embedded a depth of 25mm in the sand foundation. Sand was glued to the base of the structure to prevent slip between the base of the structure and the sand foundation.

The foundation was constructed of Leighton Buzzard Sand passing BSS No. 52 and retained on BSS No. 100. The mean grain size is therefore 0.225mm.

During tests, the model experienced a nominal centrifugal acceleration of 80 g. The model therefore simulated a structure approximately 8.6m high by 12m wide embedded 2m in the foundation sand.

The model structure was subjected to simulated earthquake loading under two foundation conditions, dry (RSS110) and saturated (RSS111). For the dry sand test the relative density of the foundation sands, D_r, was estimated to be $D_r = 64\%$.

For the tests using a saturated sand foundation, de-aired silicon oil with a viscosity of 80 centistokes was used as a pore fluid. The initial relative density of the saturated sand foundation was $D_r = 52\%$. In the gravitational field of 80g, the structure underwent consolidation settlement which led to an increase in density under the structure compared to that in the free field. This change in density was taken into account in the analysis.

RESPONSE OF EMBEDDED STRUCTURE IN DRY SAND FOUNDATION

The complete instrumentation of the model structure is shown in Fig. 12. The input motion was measured by ACC 3441 mounted on a concrete base supporting the model container. Accelerometers ACC 1925, ACC 1552 and ACC 1572 measured vertical accelerations; all other accelerometers measured horizontal accelerations.

Model Response in Test RSS110

Model responses to a simulated earthquake are shown in Fig. 13. ACC 1925 and ACC 1552, which were located in the sand foundation, show large baseline shifts and were not used in the study. These shifts may be due to drifts caused by poor earth connection (Steedman 1986). It is also probable that the gauges rotated so that they measured a mixture of vertical and horizontal accelerations. ACC 1572 is also highly suspect because of the large baseline shift and the very noisy response. All accelerometer responses contain some high frequency noise and therefore were filtered using a 10 Hz low pass filter.

The input motion measured by ACC 3441 is shown in Fig. 14 along with the baseline corrected motion at prototype scale. The baseline corrected motion was used as the input for the TARA-3 analysis.

Comparison of Computed and Recorded Accelerations: RSS110

Computed and recorded acceleration time histories from both centrifuge model studies RSS110 and RSS111 are compared on the basis of peak acceleration, distribution of amplitudes and frequency content. The effects of the accelerations on the structure depend on all these factors and for many soil structures the damage potential is very strongly dependent on the last two. If the peak acceleration is associated with very high frequency motion, such as a narrow spike, then its influence on the response of the soil structure may not be very significant. Therefore, although comparisons on the basis of peak accelerations are the easiest to make, they can be very misleading if the computed and recorded acceleration records are otherwise quite dissimilar. Therefore the comparisons which follow are based on the entire acceleration time-histories.

The computed and measured peak accelerations expressed as a percentage of gravity are given in Table 4.

Table 4 Comparison of Peak Accelerations in Test RSS110

Transducer No.	Measured (%g)	Computed (%g)
ACC 3479	6.41	6.21
ACC 3466	7.10	6.50
ACC 3477	7.06	6.50
ACC 3478	10.6	7.42
ACC 3457	10.5	6.95
ACC 1225	11.6	6.88
ACC 1938	10.1	8.89
ACC 1572	3.79	3.76

The measured and computed accelerations at the locations of ACC 3479, ACC 3466 and ACC 3477 are shown in Fig. 15 through Fig. 17. In each case the computed and measured acceleration records agree closely in peak accelerations, predominant frequency content and in the distribution of amplitudes.

The computed and measured horizontal accelerations at the top of the structure at the location of ACC 1938 are shown in Fig. 18. The peak accelerations and the distribution of amplitudes in both records agree closely. The predominant frequency of each record corresponds to the frequency of the input motion.

The vertical accelerations due to rocking as recorded by ACC 1572 and those computed by TARA-3 are shown in Fig. 19. Again, the computed accelerations closely match the recorded accelerations in both peak values and frequency content. Note that the frequency content of the vertical accelerations is much higher than that of either the horizontal accelerations at the same level in the structure or that of the input motion. This occurs because the foundation soils are much stiffer under the normal compressive stresses due to rocking than under the shear stresses induced by the horizontal accelerations.

ACC 3478, ACC 3457 and ACC 1225 show uncharacteristically strong high frequency response superimposed on the predominant frequency of the input

motion. The peak acceleration is associated with a narrow spike in all three records as shown in Fig. 20 through Fig. 22. The over-riding high frequency may be coming from the rocking motions of the structure. The accelerometers may not be exactly horizontal and therefore are picking up some of the vertical accelerations. Due to the high frequency over-ride, predicted accelerations are less than those recorded.

Comparison of Measured and Computed Settlements: RSS110

The settlements were measured at two locations on top of the structure by LVDT 81648 and LVDT 77452 and on the sand surface by LVDT 48411 and LVDT 92032 as shown in Fig. 12. The recorded and measured settlements are given in Table 5.

Table 5 Comparison of Settlements in Test RSS110

Transducer No.	Measured (mm)	Computed (mm)
48411	2.4	3.6
81648	3.2	3.1
77452	3.2	3.5
92032	2.4	4.4

In keeping with the experience in previous tests (Finn, 1987), the settlements of the structure were predicted satisfactorily. Agreement between measured and computed settlements of the sand surface are less satisfactory, again in line with previous experience. This is due in part to the difficulty in measuring settlements on the free sand surface using LVDTs. Irregularities in the surface and local variations in density, which are magnified by the centrifugal scaling factor, create uncertainty in the recorded measurements. Irregular settlements of the sand surface during the period when the centrifuge is reaching its operating speed also have an effect, including possible inclination of the pads under the LVDTs.

The computed settlement pattern is depicted in Fig. 23 and the measured values are also shown. The settlements are plotted with a magnification of 300.

RESPONSE OF EMBEDDED STRUCTURE IN SATURATED SAND FOUNDATION

The locations of the accelerometers (ACC), pressure transducers (PPT), and LVDTs are shown in Fig. 24. Analyses of previous centrifuge tests (Finn, 1987) indicated that TARA-3 was capable of modelling acceleration response satisfactorily. Therefore, in the present test, more instrumentation was devoted to obtaining a good data base for checking the ability of TARA-3 to predict residual porewater pressures.

As may be seen in Fig. 24, the porewater pressure transducers are duplicated at corresponding locations on both sides of the centreline of the model except for PPT 2255 and PPT 1111. The purpose of the duplication was to test the reliability of the data and the homogeneity of the model. If the model were homogeneous and the instrumentation perfect, then responses measured by corresponding pairs of transducers would be similar. Then any inability to model the data should be attributed to deficiencies in analysis. Duplication was not possible in previous tests because of limited data channels and in some cases it was difficult to decide whether differences between measured and computed responses were due to instrumentation problems, inhomogeneity of foundation properties or deficiencies in analysis.

Model Response in Test RSS111

Smoothed response data from all transducers are shown in Fig. 25 and Fig. 26. The input motion was recorded by ACC 3441. Note that the record ACC 3441 appears in both data sets and the two smoothed records, though very similar, show some difference, including a 1%g difference in peak acceleration due to smoothing recordings of ACC 3441 from different tapes. This example shows the susceptibility of recorded data to minor perturbations, something that should be kept in mind when reviewing comparisons between computed and recorded data.

Accelerometers ACC 1552, ACC 1925, ACC 1900 and ACC 1572 measured vertical accelerations. All other accelerometers measured horizontal accelerations.

ACC 1925 located adjacent to the edge of the structure shows significant response even after the simulated earthquake had ceased (Fig. 25) and was not taken into consideration during this study. Neither was ACC 1552 (Fig. 25) which shows a large baseline shift and a fundamental frequency comparable to

that of the input motion instead of the much higher frequencies usually associated with vertical accelerations in these kinds of tests. It is probable that the accelerometer rotated so that it measured a combination of vertical and horizontal accelerations. ACC 3457 also shows a large baseline shift which was corrected before using the record in the study.

ACC 1900 and ACC 1572 are located on opposite edges of the top of the structure. One would expect these records to be quite similar yet they are quite different. ACC 1572 is a very noisy record compared with ACC 1900. Experience with similar tests suggests instrumentation problems with ACC 1572 whereas the response of ACC 1900 is quite typical.

The porewater pressure records, shown in Fig. 26, show the sum of the transient and residual porewater pressures. The peak residual porewater pressures were attained when the earthquake excitations ceased at about 95 milliseconds. After this, most of the records show significant decreases in pressures due to drainage. The pressures recorded by the symmetric pairs PPT 2631 and PPT 2338, PPT 2626 and PPT 2848, PPT 2628 and PPT 2851, and PPT 2855 and PPT 2846 are quite similar although there are obviously minor differences in the levels of both transient and residual porewater pressures. Therefore the sand foundation is assumed to be symmetrical in its properties about the centreline of the model.

PPT 2631 and PPT 2338 records show large oscillations about the residual porewater pressure levels. The transducers were located directly underneath the structure and therefore they were subjected to large cycles of mean normal stresses due to rocking of the structure. The fluctuations in mean normal stresses caused equal changes in porewater pressures since the sand is saturated. It is also apparent that the fluctuations in these records are 180 degrees out of phase in keeping with the fact that the cyclic normal stresses caused by rocking are 180 degrees out of the phase at these locations.

As free field is approached, the influence of soil-structure interaction is decreasing and the porewater pressure records show much smaller oscillations. Transducers PPT 2846 and PPT 2855 are close enough to the structure to be affected by the cyclic normal stresses caused by rocking.

PPT 2842 is located on the centreline of the model approximately midway between the base of the model and the base of the structure. This location is not subjected to large normal stress fluctuations due to rocking and

therefore the porewater pressure record does not oscillate much about the residual porewater pressure. However, PPT 2842 record is not consistent with other porewater pressure records or with the input motion. The strongest shaking occurs between elapsed times 50 and 75 milliseconds and strong shaking persists up to 90 milliseconds. Yet PPT 2842 shows significant drainage from time 60 milliseconds which is not evident in any other records. It is probable that drainage occurred along the lead of the transducer.

During strong shaking, PPT 1111 record show large fluctuations in pressures causing negative porewater pressures. PPT 1111 was located near the surface and adjacent to the structure. Hence, due to rocking of the structure, this was subjected to large shear strains. This, along with low confining pressure at this location, led to the strongly dilatant behaviour.

The input motion measured by ACC 3441 is shown in Fig. 27 at prototype scale. It also includes the baseline corrected motion. It can be seen that the uncorrected and corrected motions are identical. The total duration of the earthquake is around 10.0 seconds and significant shaking ceases around 7.5 seconds. The peak acceleration of 14.3%g occurs at 4.17 seconds.

The prototype was analyzed as a 2-D plane strain problem using TARA-3. The foundation sand was assumed to be symmetrical in its properties about the centreline. In the centrifugal acceleration field of 80g, the heavy structure underwent consolidation settlement which led to an increase in density under the structure compared to that in the free field. For the analysis, the soil density under the structure was adjusted to be 64% based on the consolidation settlements.

Comparison of Computed and Measured Accelerations: Test RSS111

The measured and computed accelerations at locations of ACC 3479, ACC 3466 and ACC 3478 are shown in Fig. 28 through Fig. 30. Measured and computed responses at the location of ACC 3479 (Fig. 28) are similar to that of the input motion. This is expected because ACC 3479 was located very close to the base. Computed peak amplitudes closely agree with those of measured ones. The measured and computed peaks are 14.4%g and 13.3%g respectively. Comparison in terms of frequency content is also good.

At location of ACC 3466, the comparison between computed and measured acceleration is generally good both in terms of peak values and frequency content (Fig. 29). However, the computed peak ordinates between 4.0 and 6.0

seconds are somewhat less than the measured values. The measured and computed peak accelerations are 14.4%g and 11.0%g respectively.

Computed and recorded accelerations at the location of ACC 3478 are shown in Fig. 30. Peak accelerations are reasonably close (12.1%g vs 13.5%g) and the forms of the records are similar.

The measured and computed horizontal accelerations at the top of the structure at the location of ACC 1938 are shown in Fig. 31. They are very similar in frequency content, each corresponding to the frequency of the input motion given by ACC 3441 (Fig. 27). The peak accelerations agree closely with peak values of 16.9%g and 16.3%g respectively.

The computed and measured vertical accelerations at the location of ACC 1900 are shown in Fig. 32. The computed response closely matches the recorded response in both peak values and frequency content. As seen in Fig. 25, high frequency noise is present in ACC 1572 record and therefore frequency components higher than 10.0 Hz were removed by a low pass filter. The original and filtered responses are shown in Fig. 33. Fig. 34 shows the comparison between the filtered and computed responses. Both records are now very similar. The measured and computed peaks at location of ACC 1572 are 7.22%g and 6.86%g while at the corresponding location of ACC 1900 they are 6.32%g and 6.86%g respectively. The measured and computed accelerations at the location of ACC 3436 are shown in Fig. 35. ACC 3436 was located on the vertical edge of the structure that lies parallel to the plane of shaking as shown in Fig. 24. It is close to the side of the container. The records are quite similar but the computed peak accelerations are about 20% less than the recorded.

As may be seen from Fig. 24, ACC 3457 record shows a large baseline shift. The original (uncorrected) and the baseline corrected records are shown in Fig. 36. Fig. 37 shows good agreement between the corrected and the computed responses in terms of frequency content and peak values.

Comparison of Computed and Measured Porewater Pressures: Test RSS111

Computed and measured peak residual poreater pressures are given in Table 6. The computed pressures agree very closely with the measured pressures except in two locations.

Table 6 Comparison of Peak Residual Porewater Pressures in Test RSS111

Transducer No.	Measured (kPa)	Computed (kPa)
PPT 2338	33.5	33.5
PPT 2631	33.0	33.5
PPT 2848	24.5	18.0
PPT 2626	24.0	18.0
PPT 2851	24.3	26.6
PPT 2628	23.7	26.6
PPT 2846	38.1	38.0
PPT 2855	36.0	38.0
PPT 2342	-	72.0
PPT 2255	37.0	38.0
PPT 1111	4.0	2.9

The measured and computed porewater pressures at locations of PPT 2338 and PPT 2631 are shown in Fig. 38 and Fig. 39 respectively. These transducers were located directly beneath the structure and symmetrically about the centerline. The measured responses have two types of oscillations superimposed on the steady accumulating residual porewater pressures. The low frequency oscillations are due to fluctuations in mean normal stresses caused by rocking of the structure and the higher frequency peaks superimposed on these are due to dilations caused by shear strains. However, the computed responses do not have any of these oscillations because only residual porewater pressures are computed by TARA-3. The residual porewater pressures at both locations matches the measured very well. The maximum residual porewater pressure is observed between 7.0 and 7.5 seconds just after the strong shaking has ceased and before significant drainage has time to occur. The measured and computed residual porewater pressures at both locations are 16.0% of the initial effective vertical stress.

The pair PPT 2848 and PPT 2626 are located symmetrically about the centreline outside the edge of the structure at the same elevation as the pair PPT 2338 and PPT 2631. The measured and computed pressures are shown in Fig. 40 and Fig. 41 respectively. The pressures measured at these locations show somewhat smaller oscillations than those recorded under the structure. This is due to the fact that the effects of rocking on mean normal streses at these locations is less than at locations under the structure. At these locations, the computed residual porewater pressures are somewhat less than the measured ones but the overall agreement is quite satisfactory.

It is interesting to note that measured PPT 2848 response shows a slight increase in pressures in the range 7.5 to 8.2 seconds before showing a decrease in pressures. This increase is thought to have occurred due to migration of porewater pressures from surrounding areas of high porewater pressure such as the location of PPT 2338.

Figs. 42 and 43 show the computed and measured of porewater pressure responses at the locations of PPT 2846 and PPT 2855 respectively. In both cases, the comparison is excellent both in terms of the rate of development and peak residual value. The measured and computed peak residual porewater pressures, agree closely. The drop in recorded pressure after 7.5 sec is due to drainage after significant shaking had ceased. This post-earthquake drainage was not analysed.

The pair PPT 2851 and PPT 2628 were located out in the free field at the same elevation as the pair PPT 2338 and PPT 2631 and the responses at these locations are compared in Fig. 44 and Fig. 45 respectively. The measured peak residual porewater pressure is slightly less than the computed one but the overall agreement is good. The large oscillations observed in the PPT 2338 and PPT 2631 responses are absent here indicating that the influence of soil-structure interaction is not significant at these locations.

PPT 2842 is located on the centreline, midway between the base of the model and base of the structure. Computed and measured porewater pressures shown in Fig. 46 agree closely for the first 5.0 seconds of the record and then deviate sharply. As discussed earlier, the measured pressures are not compatible with all other records or the input motion. The record shows significant drainage after 5.0 seconds. The only possible reason for such drainage during the strongest shaking in the range 4.0 to 6.0 seconds is that a drainage path developed along the cable to the transducer PPT 2842. The

computed pressures show a steady increase in the range 4.0 to 6.0 seconds consistent with the input. The demonstrated homogeneity of the model about the centreline and the close agreement between measured and computed porewater pressures for all other transducers support the notion that the behaviour of PPT 2842 is anomalous.

Fig. 47 compares responses at the locations of PPT 2255 which was located out in the free field directly below PPT 2628. Computed and measured pressures at this location agree very well for the first 7.0 seconds. The measured response shows significant drainage after 7.0 seconds. The post-earthquake drainage was not analysed.

The contours of peak residual porewater pressures computed by TARA-3 are shown in Fig. 48. The integers are the contour values in kPa. The triangles show the locations where the porewater pressures were measured and the associated numbers indicate the measured peak residual pressures. The figure demonstrates the overall agreement between the measured and computed values and the symmetric nature of the contours.

Stress-Strain Behaviour

Computed shear stress-strain responses at selected locations are presented in this section to illustrate the effects of soil-structure interaction and porewater pressures on stress-strain responses. Figs. 49 and 50 show stress-strain responses at the locations of PPT 2338 and PPT 2842 respectively. At these locations, hysteretic behaviour is evident but the response for the most part is only mildly nonlinear. The initial effective stresses under the structure are high and therefore the initial shear moduli are high. The seismic porewater pressure ratios, u/σ'_{yo}, are only 16% and 24%.

The response in the free field at the location of PPT 2851 (Fig. 51) is strongly nonlinear with large hysteresis loops. This indicates considerable softening due to high porewater pressures and shear strains. At this location, the porewater pressure ratio reached about 80%. The stiffer loops found in the response are associated with the initial stages of the shaking where very low porewater pressure were generated. However, as the shaking continued, high porewater pressures are generated and as a result the shear modulus and shear strength are reduced giving rise to the softer and flatter hysteretic loops.

A similar type of response was computed at location of PPT 2848 (Fig. 52) where the porewater pressure ratio was about 66% and at the location of PPT 2846, where the porewater pressure ratio reached a level of 65% (Fig. 53).

Comparison of Displacements in Test RSS111

The measured and computed displacements at the locations of LVDT 1648 and LVDT 4457 (Fig. 24) are given in Table 7 at prototype scale. LVDT 1648

Table 7 Comparison of Displacements in Test RSS111

Transducer No.	Measured (m)	Computed (m)	Direction
LVDT 1648	0.012	0.020	Vertical
LVDT 4457	0.0016	0.006	Horizontal

was mounted at the left hand top edge of the structure to measure vertical settlement while LVDT 4457 measured horizontal displacement.

The differences between measured and computed deformations may be due to the approximate nature of the values of the volume change constants C_1 to C_4 used in the analysis. They were derived from a correlation analysis using the liquefaction resistance curve for D_r = 52%. However this curve was not determined experimentally but derived from the experimental liquefaction curve for D_r = 64% by direct proportioning according to relative density.

Note that the computed settlements of the same structure in test RSS110 in which the sand has a relative density D_r = 64% compared very closely with the measured settlements. In this case, the constants C_1 to C_4 were obtained by correlation using the experimental liquefaction curve for D_r = 64%.

There is some uncertainty about the reliability of the measured settlements in test RSS111. During swing up LVDT readings suggested a pronounced clockwise rotation of the structure which is unexpected since subsequent porewater pressure measurements indicated that the sand embankment was very homogeneous. The accuracy of the readings cannot be confirmed because deformations were not measured at any other location on the structure.

The final deformation pattern as computed by TARA-3 is shown in Fig. 54. The dotted line shows the undeformed shape and the solid line shows the final deformed shape. It should be noted that the deformations are magnified about 10 times. The top surface of the sand foundation settles more than the structure. Also, at the lower end of the sloping faces, the sand bulges out on both sides. This is close to the constant volume type of deformation often found in fully saturated sand embankments.

CONCLUSIONS AND RECOMMENDATIONS

The comparison between measured and computed responses of the centrifuged model structures embedded in saturated and dry sand foundations demonstrates the wide ranging capability of TARA-3 for performing complex effective stress soil-structure interaction analysis with acceptable accuracy for engineering purposes. Seismically induced residual porewater pressures are satisfactorily predicted even when there are significant effects of soil-structure interaction. Computed accelerations are in good agreement with measured accelerations in magnitude, frequency content and distribution of peaks. In particular, the program was able to model the high frequency rocking vibrations of the model structures. This is an especially difficult test of the ability of the program to model soil-structure interaction effects.

The effects of porewater pressures on stress-strain response are clearly evident in the computed stress-strain loops at different locations in the foundations. In the free field of the saturated foundation, where the pore pressures were very high, large hysteresis loops were computed showing strongly nonlinear response and considerable softening due to the high porewater pressures and associated high shear strains. In areas of the foundation where the porewater pressures were relatively low compared to the overburden pressures, the response was almost elastic.

This study demonstrates the utility of centrifuge modelling in providing a comprehensive data base for validating methods of seismic response analysis. Phenomenological aspects of soil-structure interaction are clearly demonstrated such as high frequency rocking response, the effects of rocking on porewater pressure patterns and the distortion of free-field motions and porewater pressures by the presence of a structure. In no other way can such

complete data coverage of acceleration and porewater pressure fields be obtained when required and at such a low cost.

Reliability of the data is best assured by duplicating sensors about the axis of symmetry of the structure. This was not done in earlier tests and in some cases it was difficult to decide whether differences between measured and computed responses were due to instrumentation problems, lack of homogeneity in the sand foundation or deficiencies in the method of analysis.

Further significant improvements in the 2-D version of TARA-3 are unlikely. In view of the demonstrated capability of the method of analysis, in two dimensions, it would appear useful to develop a 3-D version of TARA-3 to allow the direct modelling of 3-D problems.

REFERENCES

1. Barton, Y.O. (1982). Laterally Loaded Model Piles in Sand; Centrifuge Tests and Finite Element Analyses, Ph.D. Thesis, Cambridge University, Engineering Department.

2. Byrne, P.M. (1981). Class Notes: Numerical Methods in Soil Mechanics (CE573). University of British Columbia, Vancouver, B.C., Canada.

3. Byrne, P.M. and Cheung, H. (1984). Soil Parameters for Deformation Analysis of Sand Masses. Soil Mechanics Series No. 81, Department of Civil Engineering, University of British Columbia, Vancouver, B.C., Canada.

4. Byrne, P.M. and Janzen, W. (1984). INCOIL: A Computer Program for Nonlinear Analysis of Stress and Deformations in Oil Sand Masses. Soil Mechanics Series No. 80, Dept. of Civil Engineering, University of British Columbia, Vancouver, Canada.

5. Chang, C.S. (1982). Residual Undrained Deformation from Cyclic Loading. Journal of the Geotechnical Engineering Division, ASCE, Vol. 108, GT4, April, pp. 637-646.

6. Chern, J.C. (1981). Effect of Static Shear on Resistance to Liquefaction. M.A.Sc. Thesis, The University of British Columbia, Vancouver, May.

7. Desai, C.S. and Christian, J.T. (1979). Numerical Methods in Geotechnical Engineering. McGraw Hill Book Co., New York, U.S.A.

8. Dikmen, S.U. and Ghaboussi, J. (1984). Effective Stress Analysis of Seismic Response and Liquefaction: Theory, Journal of the Geotech. Eng. Div., ASCE, Vol. 110, No. 5, Proc. Paper 18790, pp. 628-644.

9. Duncan, J.M., Byrne, P.M., Wong, K.S. and Mabry, P. (1978). Strength, Stress-Strain and Bulk Modulus Parameters for Finite Element Analyses of Stresses and Movements in Soil Masses. Report No. UCB/GT/78-02, April.

10. Duncan, J.M., Byrne, P.M., Wong, K.S. and Mabry, P. (1980). Strength, Stress-Strain and Bulk Modulus Parameters for Finite Elements Analyses of Stresses and Movements in Soil Masses. Report No. UCB/GT/80-01, August.

11. Eyton, D.G.P. (1982). Triaxial Tests on Sand With Viscous Pore Fluid. Part 2, Project Report, Engineering Department, Cambridge University, Cambridge, England.

12. Finn, W.D. Liam (1987). Soil Structure Interaction During Earthquakes: Centrifuge Model Studies and Computer Analysis. Report to European Research Office of the U.S. Army, London, England.

13. Finn, W.D. Liam and Bhatia, S.K. (1980). Verification of Nonlinear Effective Stress Model in Simple Shear, Application of Plasticity and Generalized Stress-Strain in Geotechnical Engineering, ASCE, Editors, R.N. Yong and E.T. Selig, pp. 241-252.

14. Finn, W.D. Liam, and Gohl, W.B. (1987). Centrifuge Model Studies of Piles Under Simulated Earthquake Lateral Loading. Proceedings, Dynamic Response of Pile Foundations-Experiment, Analysis and Observation, Geotechnical Special Publication 11, ASCE Convention, Atlantic City, New Jersey, April 27.

15. Finn, W.D. Liam, Iai, S. and Ishihara, K. (1982). Performance of Artificial Offshore Islands Under Wave and Earthquake Loading: Field Data Analyses, Proceedings of the 14th Annual Offshore Technology Conference, Houston, Texas, May 3-6, Vol. 1, OTC Paper 4220, pp. 661-672.

16. Finn, W.D. Liam, W.K. Lee and G.R. Martin. (1976). An Effective Stress Model for Liquefaction, Journal of the Geotechnical Engineering Division, ASCE, Vol. 103, No. GT6, Proc. Paper 13008, 517-533.

17. Finn, W.D. Liam, G.R. Martin and M.K.W. Lee. (1978). Comparison of Dynamic Analyses for Saturated Sands. Proceedings of the ASCE Specialty Conference on Earthquake Engineering and Soil Dynamics. Vol. I, ASCE, New York, N.Y., pp. 472-491.

18. Finn, W.D. Liam, Pickering, J. and Bransby, P.L. (1971). Sand Liquefaction in Triaxial and Simple Shear Test. Journal of the Soil Mechanics and Foundations Div., ASCE, Vol. 97, No. SM4, Proceeding Pper 8039, April, pp. 639-59.

19. Finn, W.D. Liam, Yogendrakumar, M., Yoshida, N. and Yoshida, H. (1986). TARA-3: A Program to Compute the Response of 2-D Embankments and Soil-Structure Interaction Systems to Seismic Loadings. Department of Civil Engineering, University of British Columbia, Vancouver, Canada.

20. Goodman, R.E., R.L. Taylor and T.L. Brekke. (1968). A Model for the Mechanics of Jointed Rock, J. Soil Mech. and Found. Div. ASCE, 94 (SM3), 637-659.

21. Hardin, B.O. and Drnevich, V.P. (1972). Shear Modulus and Damping in Soils, Design Equations and Curves. Journal of the Soil Mechanics and Foundation Division, ASCE, Vol. 98, SM7, Proc. Paper 9006, July, pp. 667-692.

22. Iai, S., Tsuchida, H. and Finn, W.D. Liam (1985). An Effective Stress Analysis of Liquefaction at Ishinomaki Port During the 1978 Miyagi-Ken-Oki Earthquake, Report of the Port and Harbour Research Institute, Vol. 24, No. 2, pp. 1-84.

23. Ishihara, K. and Towhata, I. (1982). Dynamic Response of Level Ground Based on the Effective Stress Method. Ch. 7, Soil Mechanics - Transient and Cyclic Loads, Edited by G.N. Pande and O.C. Zienkiewicz, John Wiley and Sons Ltd., New York, N.Y., pp. 133-172.

24. Lysmer, J., Udaka, T., Tsai, C.F. and Seed, H.B. (1975). FLUSH: A Computer Program for Approximate 3-D Analysis of Soil-Structure Interaction Problems. Report No. EERC 75-30, Earthquake Engineering Research Center, University of California, Berkeley, California.

25. Martin, G.R., W.D. Liam Finn, and H.B. Seed. (1975). Fundamentals of Liquefaction Under Cyclic Loading, Soil Mech. Series Rpt. No. 23, Dept. of Civil Engineering, University of British Columbia, Vancouver; also Proc. Paper 11284, J. Geotech. Eng. Div. ASCE, 101 (GT5): 324-438.

26. Martin, P.P. and Seed, H.B. (1978). MASH - A Computer Program for the Nonlinear Analysis of Vertically Propagating Shear Waves in Horizontally Layered Soil Deposits. EERC Report No. UCB/EERC-78/23, University of California, Berkeley, California, October.

27. Masing, G. (1926). Eigenspannungen und Verfestigung beim Messing, Proceedings, 2nd Int. Congress of Applied Mechanics, Zurich, Switzerland.

28. Prevost, J.H., Cuny, B., Hughes, T.J.R. and Scott, R.F. (1981). Offshore Gravity Structures: Analysis, Journal of Geotechnical Engineering Division, ASCE, Vol. 107, No. GT2, pp. 143-165.

29. Schnabel, P.B., Lysmer, J. and Seed, H.B. (1972). SHAKE: A Computer Program for Earthquake Response Analysis of Horizontally Layered Sites, Report No. EERC 72-12, Earthqukae Engineering Research Center, University of California, Berkeley, California.

30. Schofield, A.N. (1981). Dynamic and Earthquake Geotechnical Centrifuge Modelling, Proceedings Int. Conf. on Recent Advances in Geot. Engineering and Soil Dynamics, St. Louis, Missouri, Vol. III: 1081-1100.

31. Seed, H.B. (1979a). Considerations in the Earthquake-Resistant Design of Earth and Rockfill Dams, 19th Rankine Lecture, Geotechnique 29, No. 3, pp. 215-263.

32. Seed, H.B. (1979b). Soil Liquefaction and Cyclic Mobility Evaluation for Level Ground During Earthquakes, Journal of Geotechnical Engineering Division, ASCE, Vol. 105, No. GT2, pp. 201-255.

33. Seed, H.B. and Idriss, I.M. (1970). Soil Moduli and Damping Factors for Dynamic Response Analysis. Report No. EERC 70-10, Earthquake Engineering Research Center, University of California, Berkeley, December.

34. Seed, H.B., I.M. Idriss and I. Arango. (1983). Evaluation of Liquefaction Potential Using Field Performance Data, Journal of Geotechnical Engineering Division, Vol. 109, No. 3, pp. 458-482.

35. Seed, H.B. and Lee, K.L. (1966). Liquefaction of Saturated Sands During Cyclic Loading. Journal of the Soil Mechanics and Foundation Engineering Division, ASCE, Vol. 96, No. SM6, November.

36. Siddharthan, R. and W.D. Liam Finn (1982). TARA-2, Two dimensional Nonlinear Static and Dynamic Response Analysis, Soil Dynamics Group, University of British Columbia Vancouver, Canada.

37. Steedman, R.S. (1986). Embedded Structure on Sand Foundation: Data Report of Centrifuge Model Tests, RSS110 and RSS111. Engineering Department, Cambridge University, Cambridge, England.

38. Tatsuoka, F., and Haibara, O. (1985). Shear Resistance Between Sand and Smooth or Lubricated Surfaces. Soils and Foundations, Vol. 25, No. 1, pp. 89-98.

39. Uesugi, M. and Kishida, H. (1986). Influential Factors of Friction Between Steel and Dry Sands. Soils and Foundations, Vol. 26, No. 2, pp. 33-46.

40. Vaid, Y.P. and Chern, J.C. (1981). Effect of Static Shear on Resistance to Liquefaction. Soil Mechanics Series No. 51, Department of Civil Engineering, University of British Columbia, Vancouver, Canada.

41. Vaid, Y.P. and Finn, W.D. Liam. (1979). Effect of Static Shear on Liquefaction Potential. Journal of the Geotechnical Engineering Division, ASCE, Vol. 105, GT10, October, pp. 1233-1246.

42. Yogendrakumar, M. and W.D. Liam Finn. (1986a). SIMCYC2: A Program for Simulating Cyclic Simple Shear Tests on Dry or Saturated Sands, Report, Soil Dynamics Group, Dept. of Civil Engineering, University of British Columbia, Vancouver, Canada.

43. Yogendrakumar, M. and Finn, W.D. Liam (1986b). C-PRO: A Program for Evaluating the Constants in the Martin-Finn-Seed Porewater Pressure Model. Soil Dynamics Group, Department of Civil Engineering, University of British Columbia, Vancouver, Canada, November.

44. Zienkiewicz, O.C. (1977). The Finite Element Method. McGraw Hill, London.

45. Zienkiewicz, O.C. and Cheung, Y.K. (1967). Finite Element Method in Structural and Continuum Mechanics. McGraw Hill Book Company.

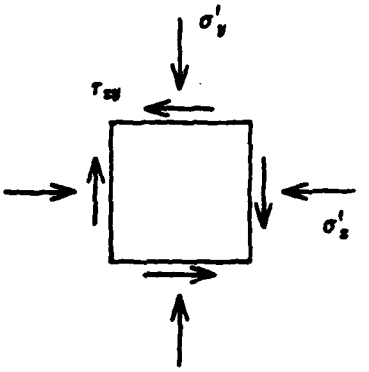

FIG. 1. General stress state in soil element.

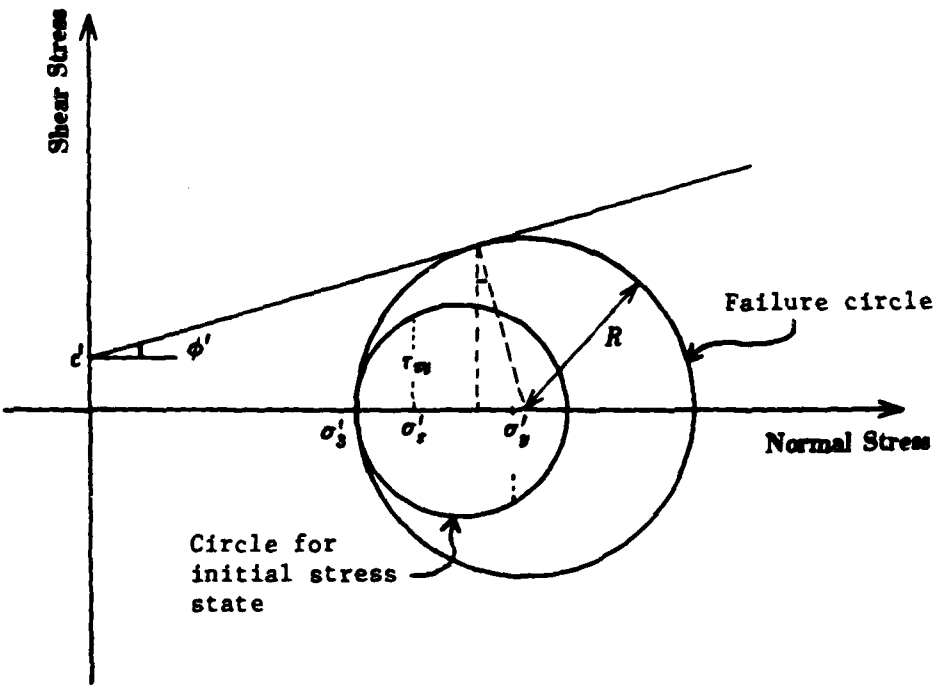

FIG. 2. Mohr circle at failure for triaxial loading conditions.

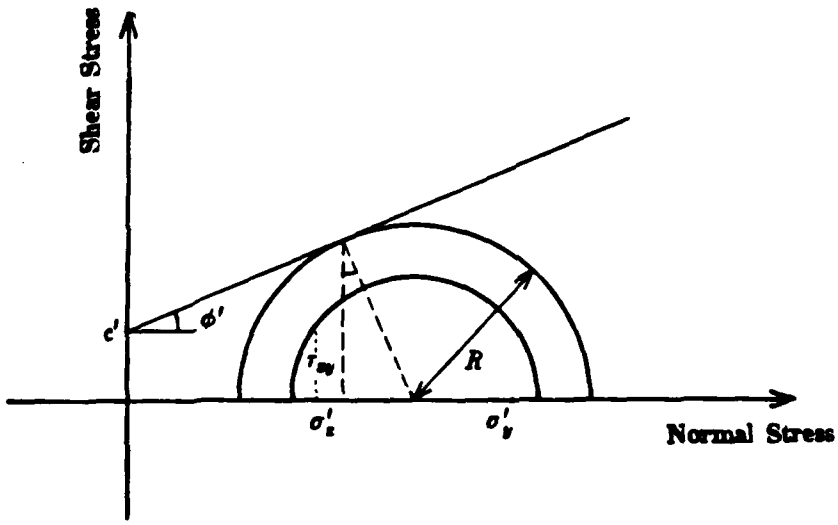

FIG. 3. Mohr circle at failure for constant mean normal effective stress loading paths.

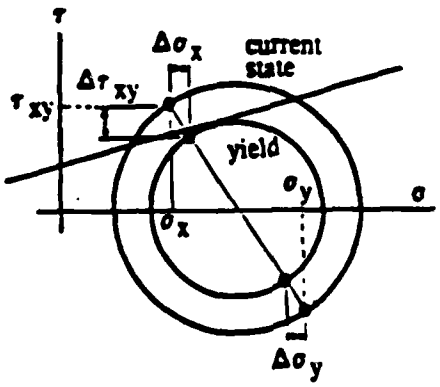

FIG. 4. Correction stresses for restoring compatibility with Mohr-Coulomb failure criterion.

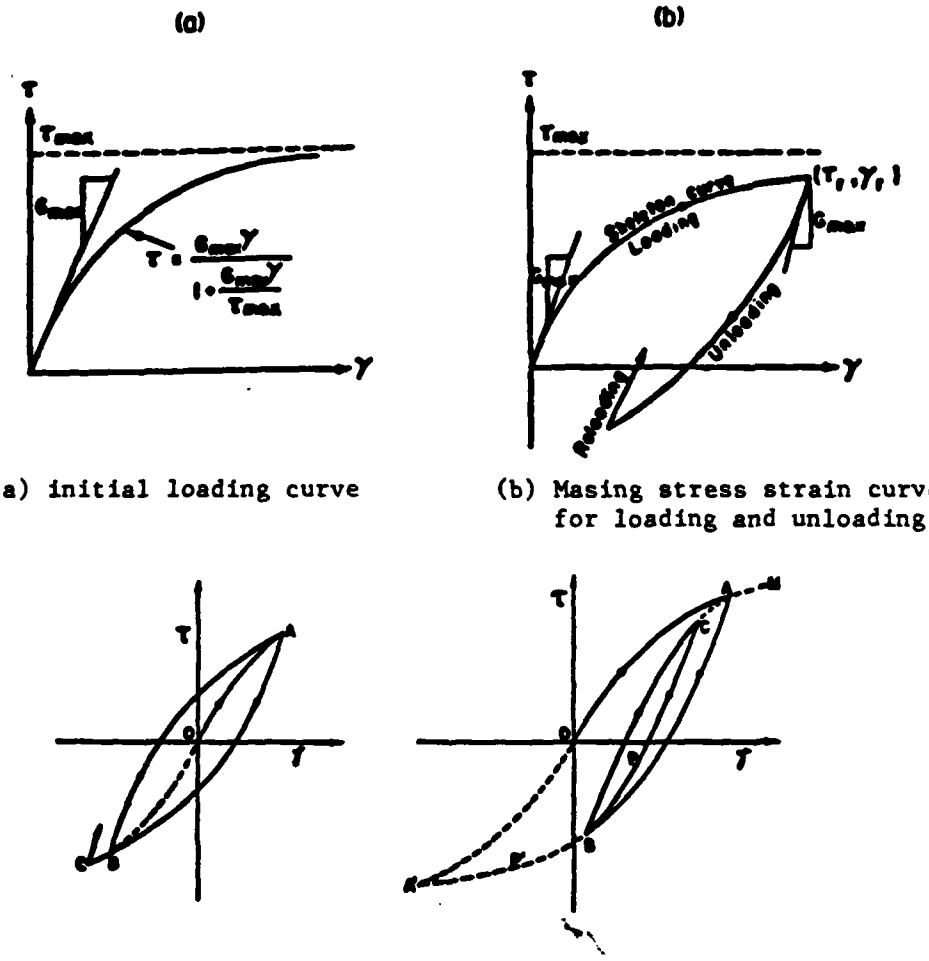

(a) initial loading curve

(b) Masing stress strain curves for loading and unloading

(c) first loading

(d) general reloading

FIG. 5. Loading paths in hysteretic stress-strain response.

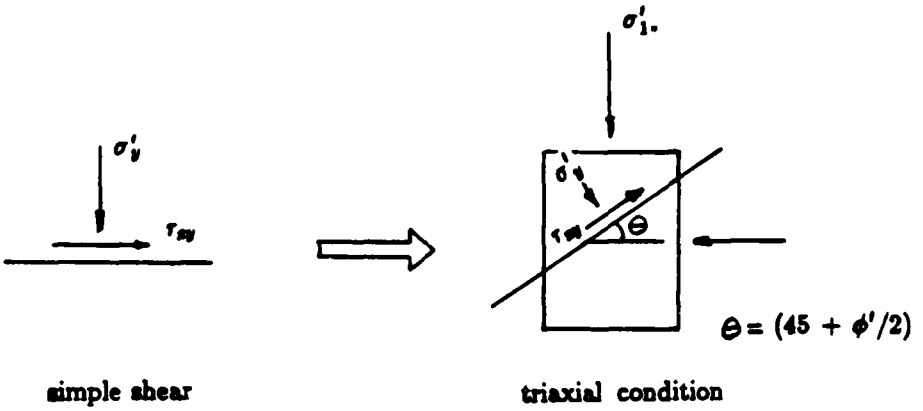

FIG. 6. Simple shear and triaxial stress conditions with equivalent stresses on the failure plane.

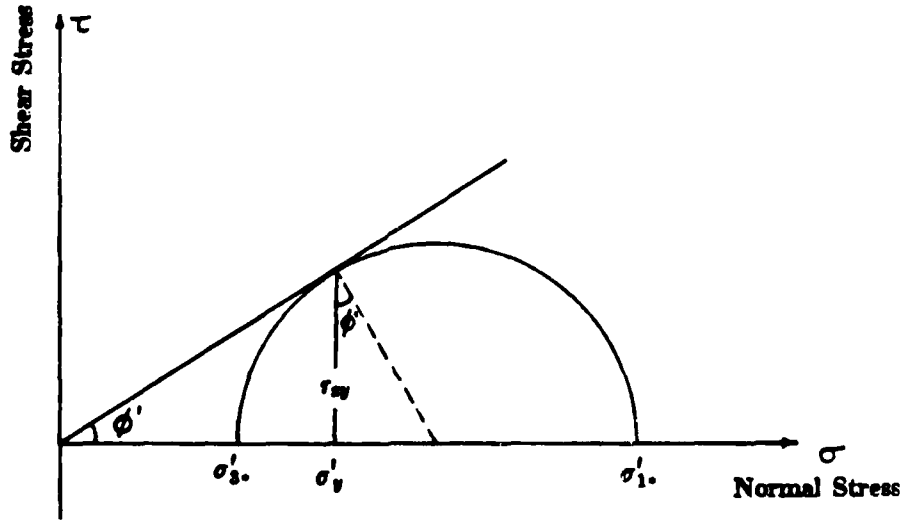

FIG. 7. Mohr circle showing equivalent triaxial stresses, σ_1^*, σ_3^* for use in criterion for limiting porewater pressure.

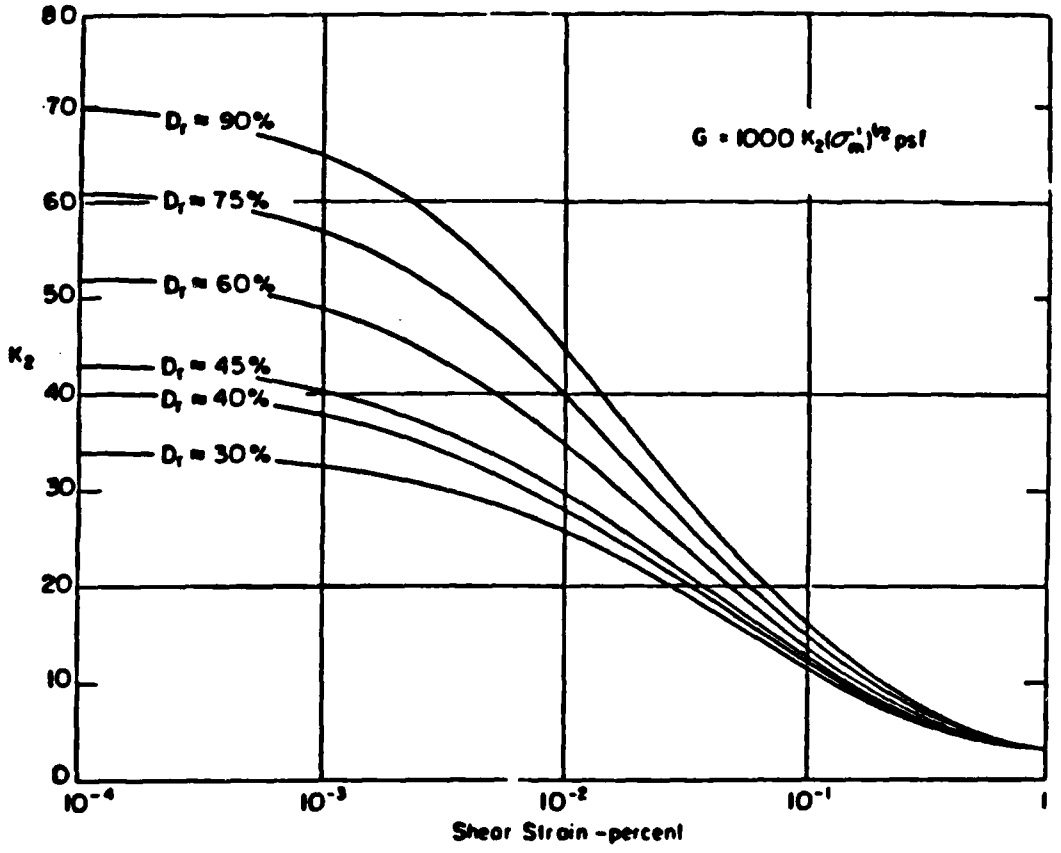

FIG. 8. Shear modulus parameter, K_2, for sands at different relative densities (Seed and Idriss, 1970).

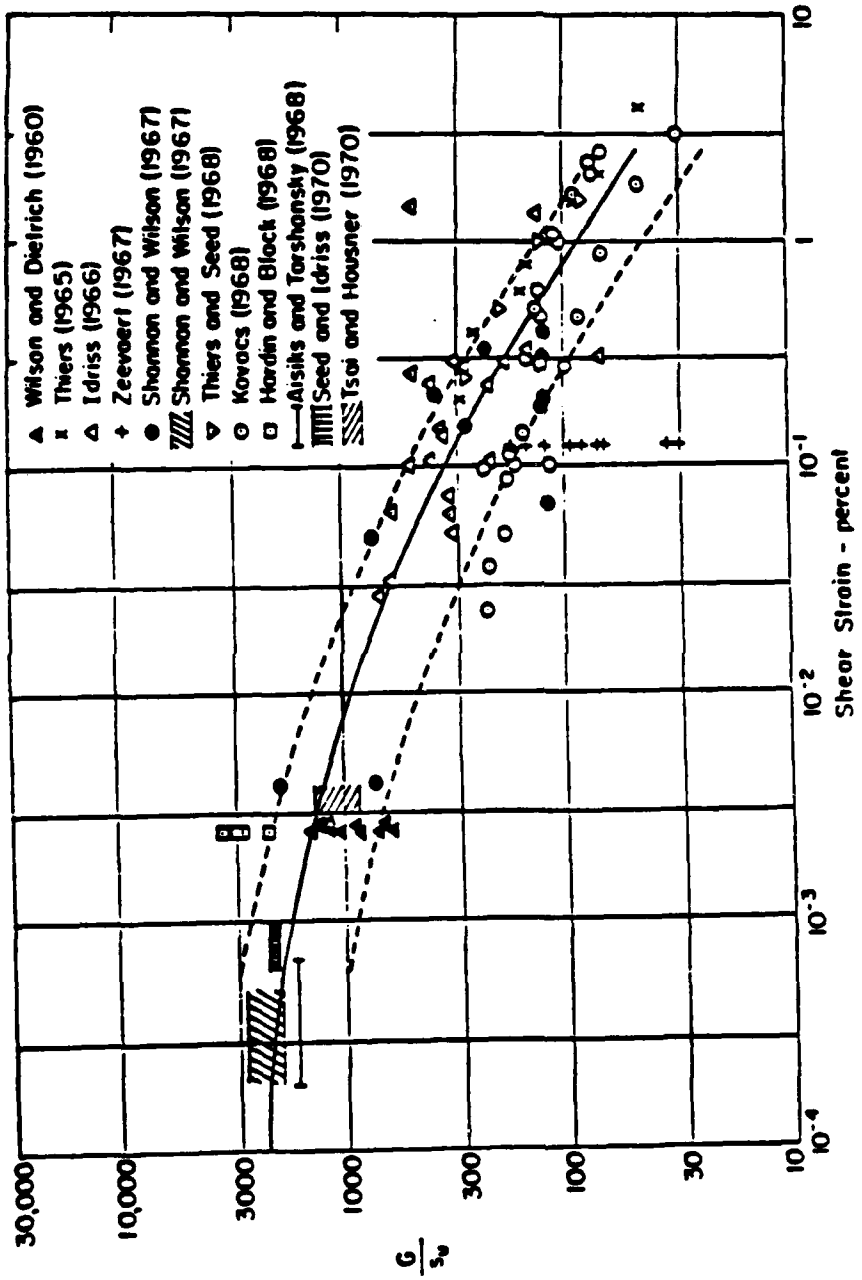

FIG. 9. Shear modull for saturated clays as a function of shear strength and shear strain (Seed and Idriss, 1970).

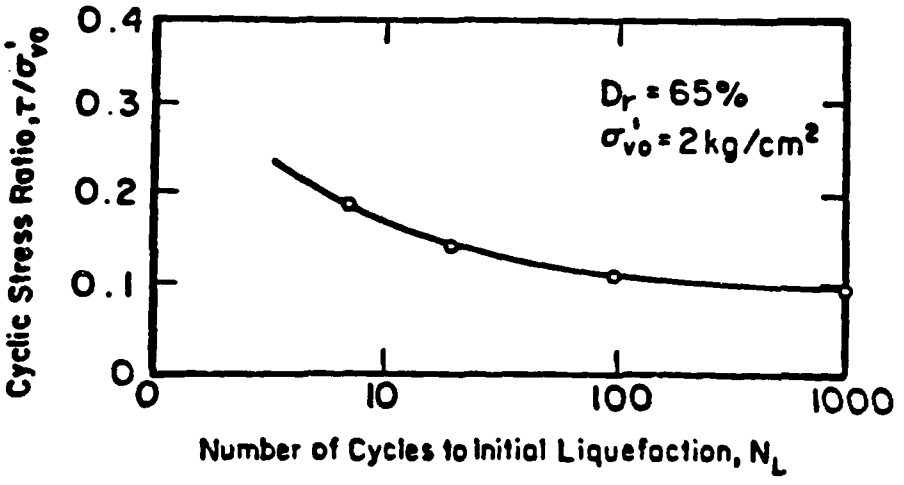

FIG. 10. Liquefaction resistance curve of Leighton Buzzard sand at D_r = 65%.

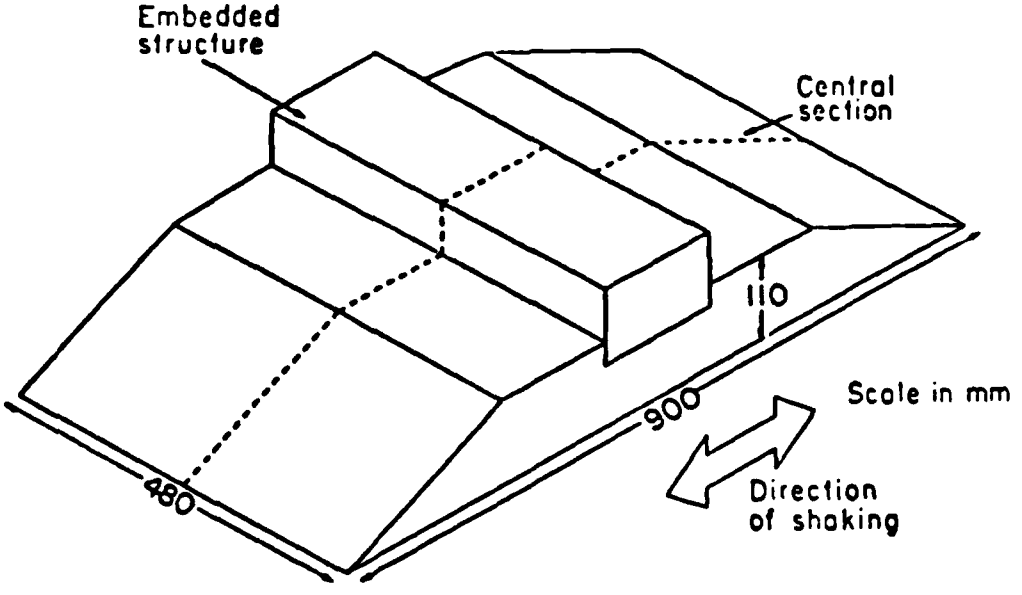

FIG. 11. Schematic view of a model embankment with embedded structure.

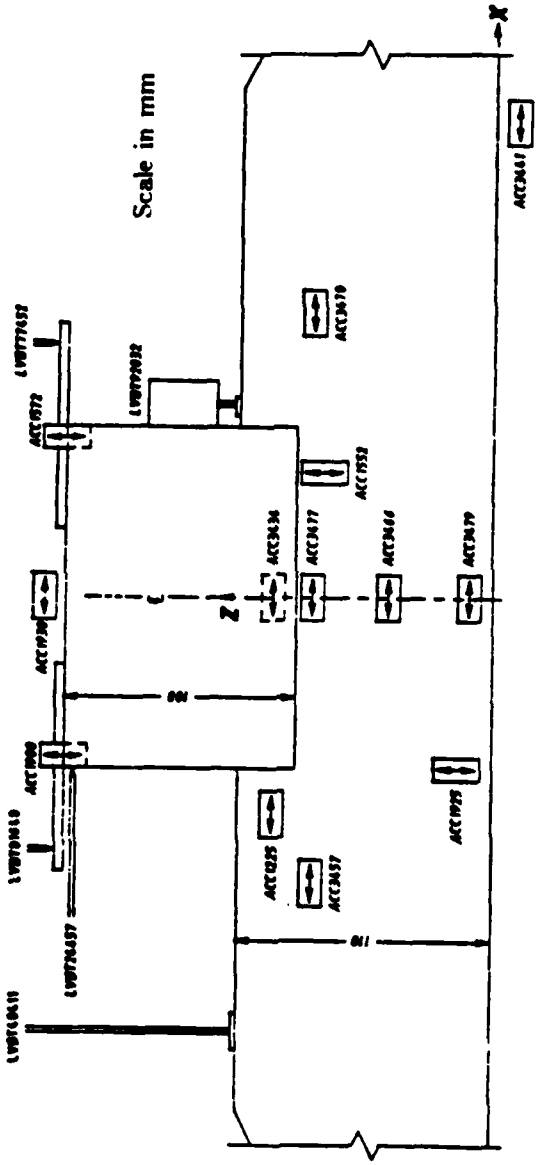

FIG. 12. Instrumentation layout in model test RSS110.

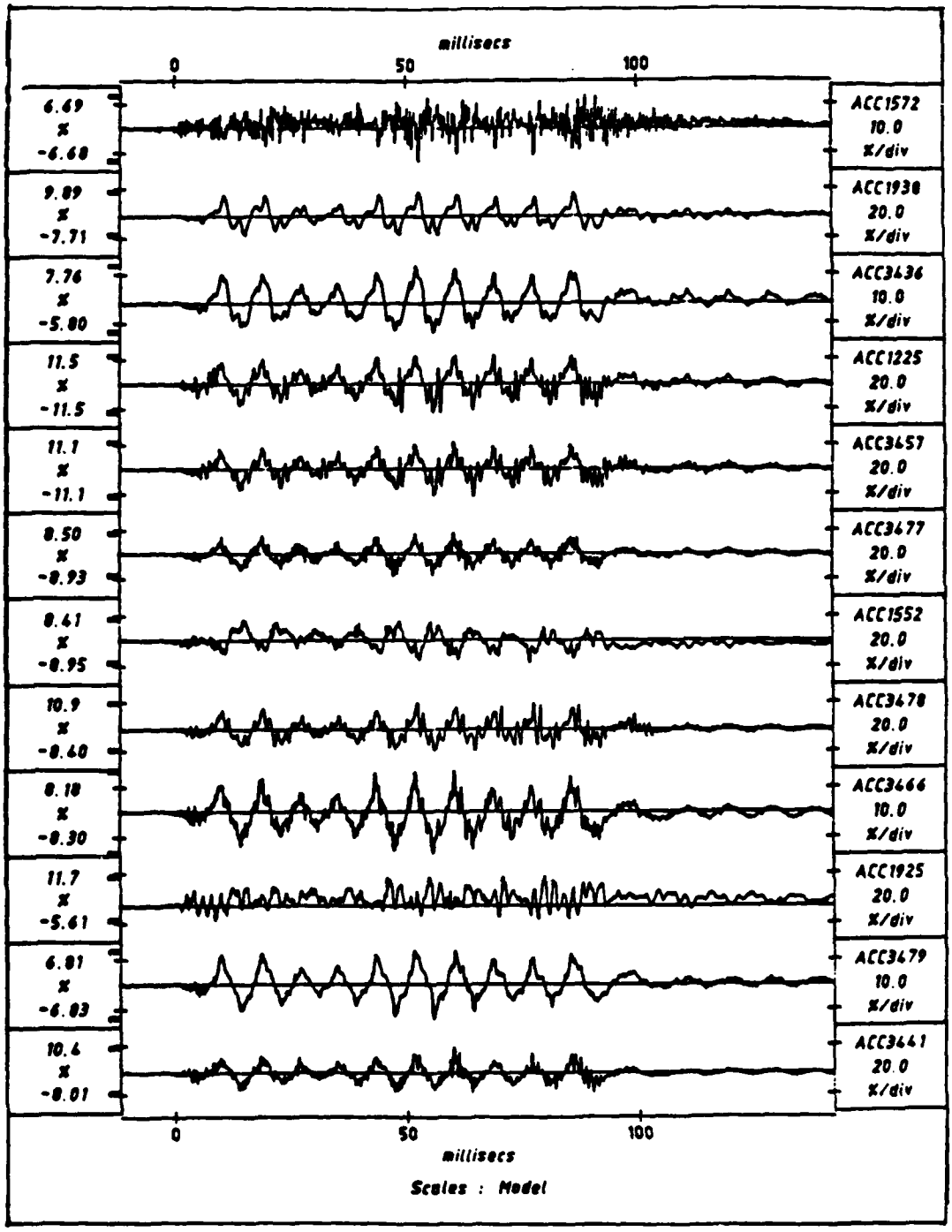

FIG. 13. Recorded accelerations in test RSS110.

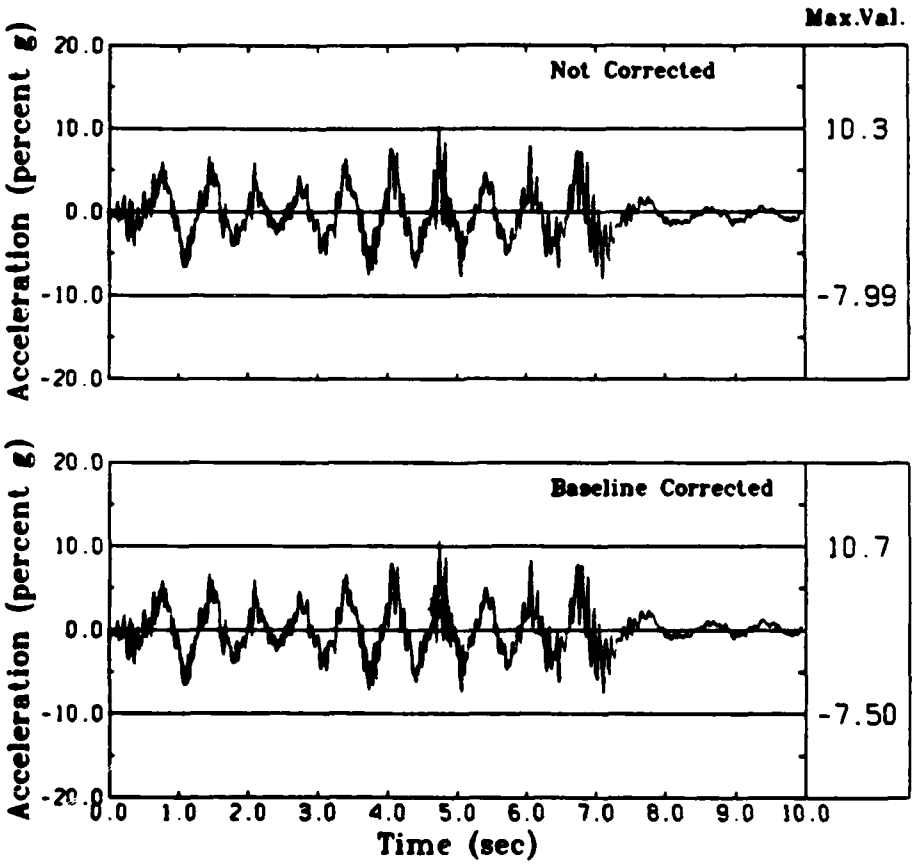

FIG. 14. Input motion for test RSS110 measured by ACC 3441.

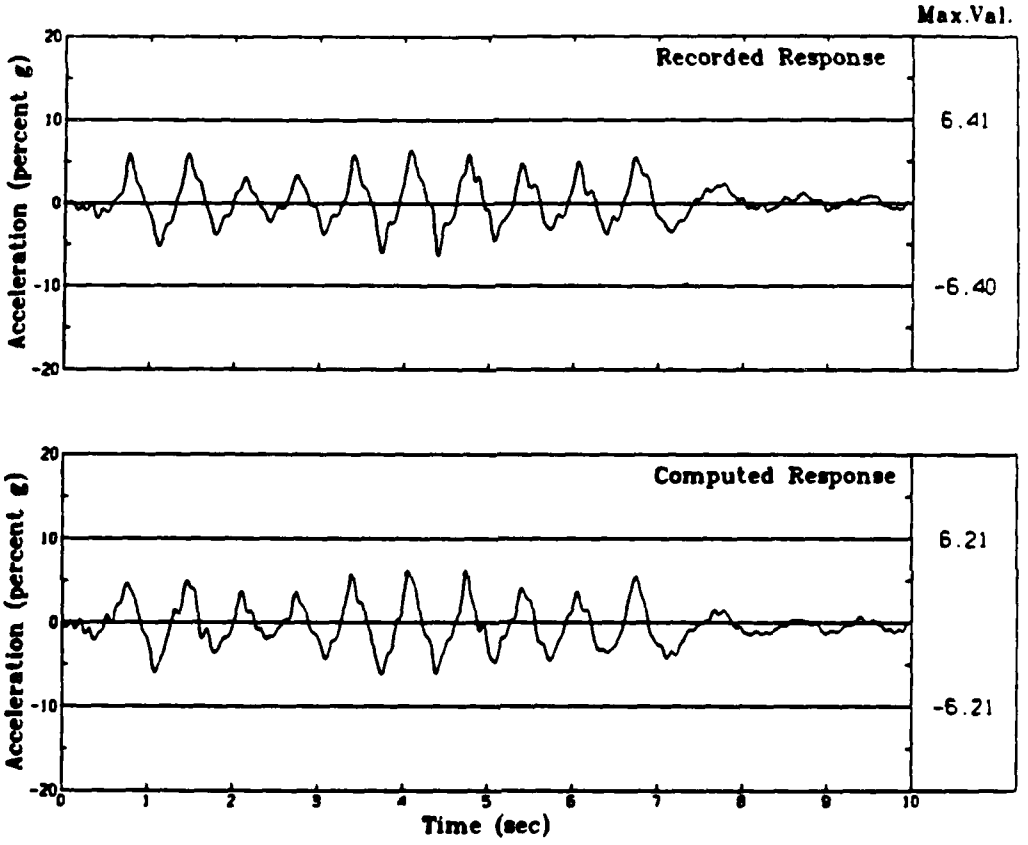

FIG. 15. Computed and measured accelerations at the location of ACC 3479 in test RSS110.

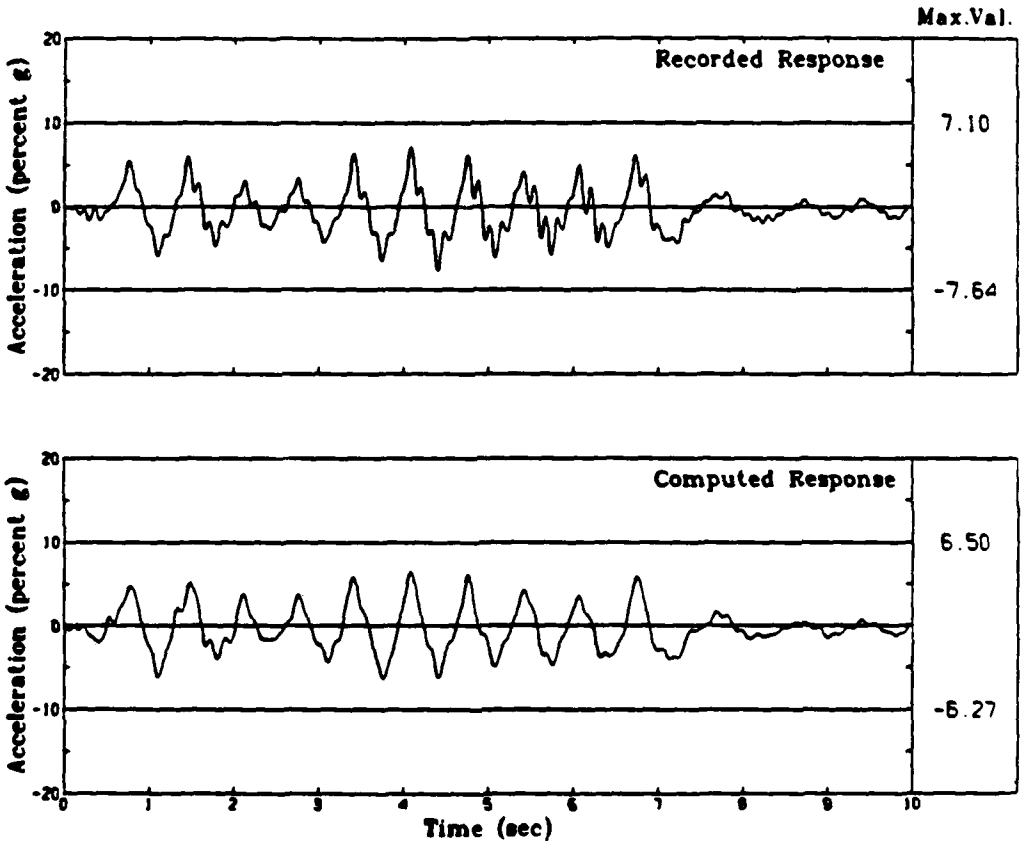

FIG. 16. Computed and measured accelerations at the location of ACC 3466 in Test RSS110.

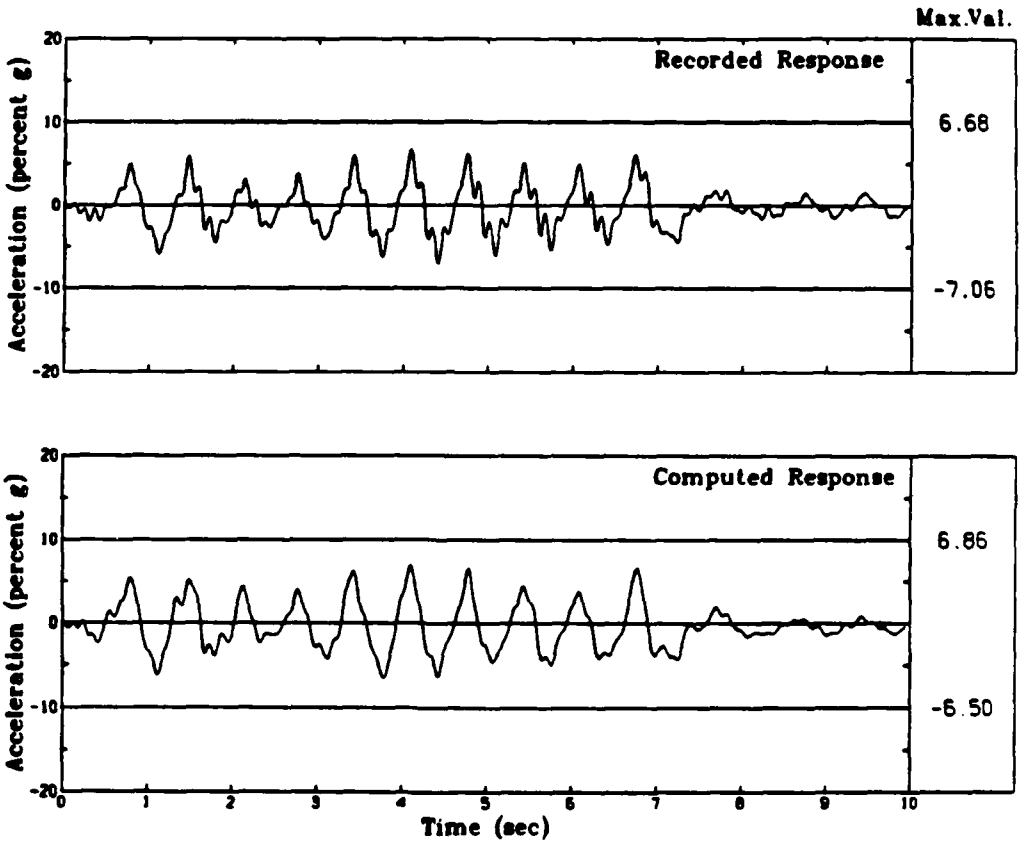

FIG. 17. Computed and measured accelerations at the location of ACC 3477 in Test RSS110.

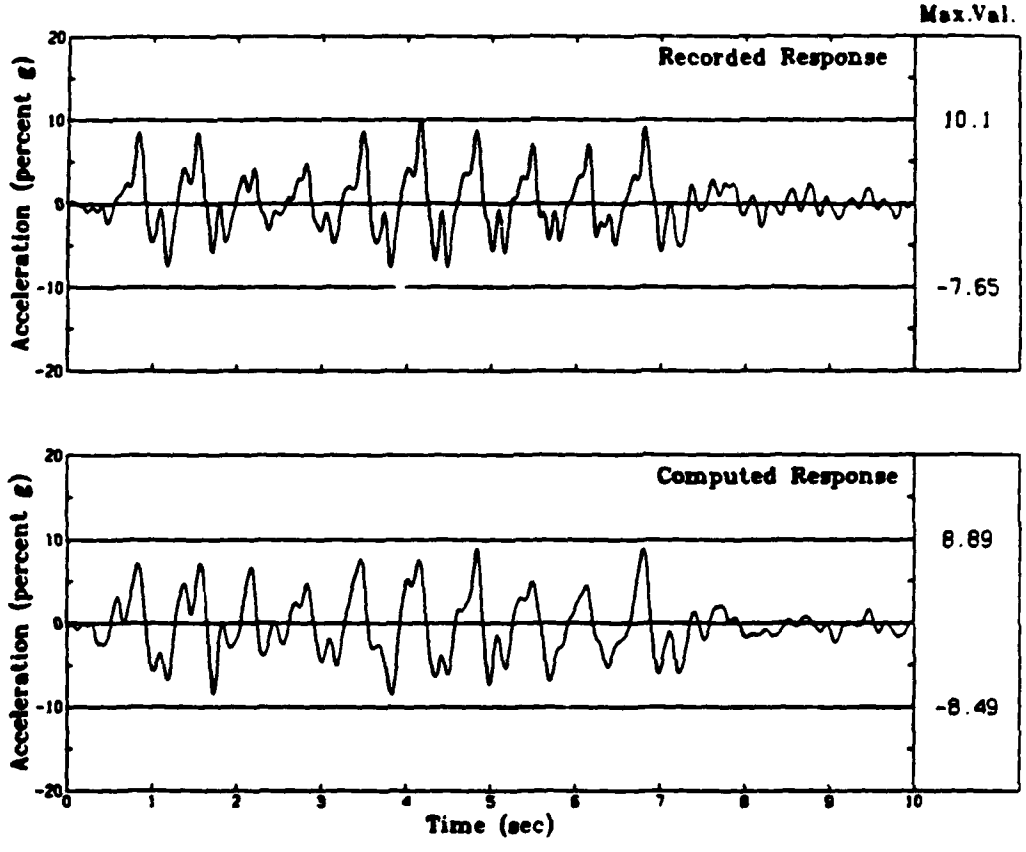

FIG. 18. Computed and measured horizontal accelerations at the location of ACC 1938 in test RSS110.

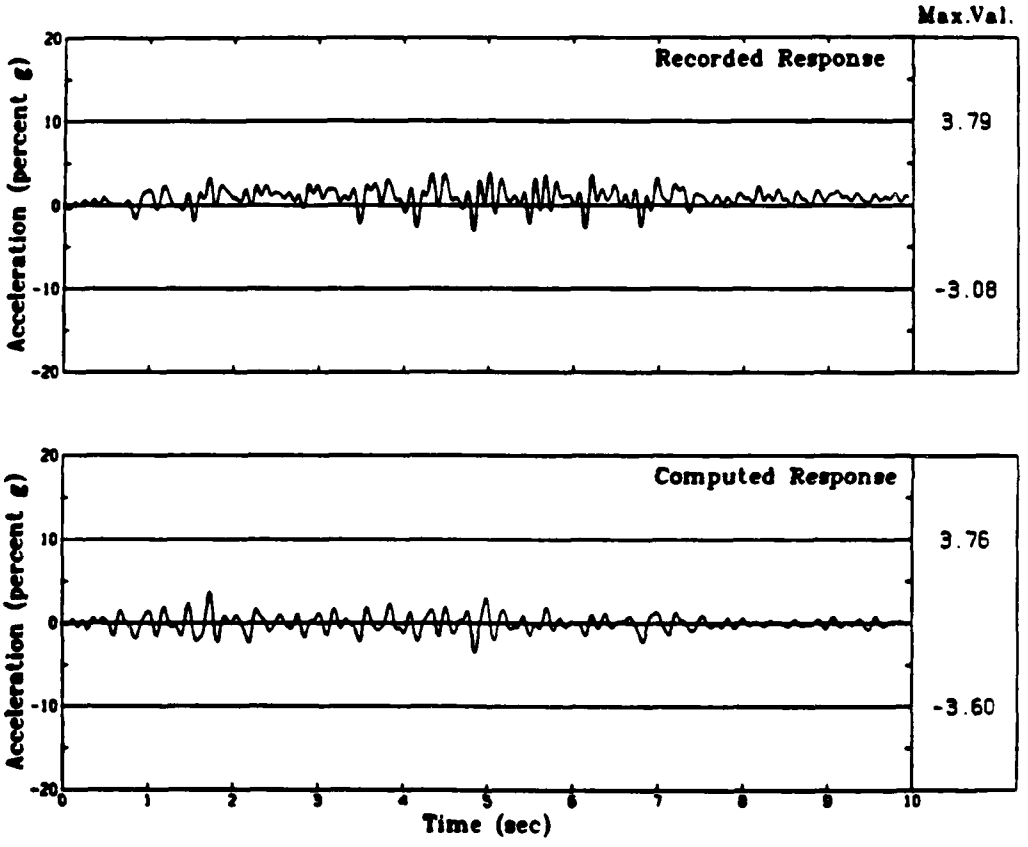

FIG. 19. Computed and measured accelerations at the location of ACC 1572 in test RSS110.

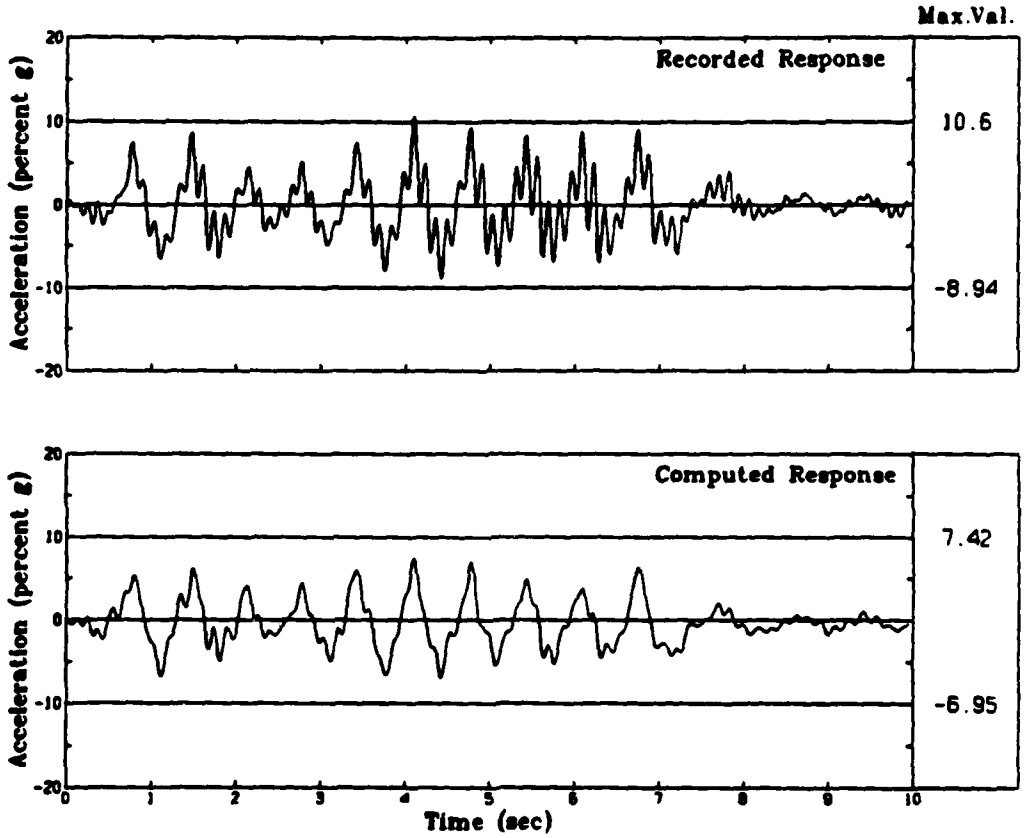

FIG. 20. Computed and measured accelerations at the location of ACC 3478 in test RSS110.

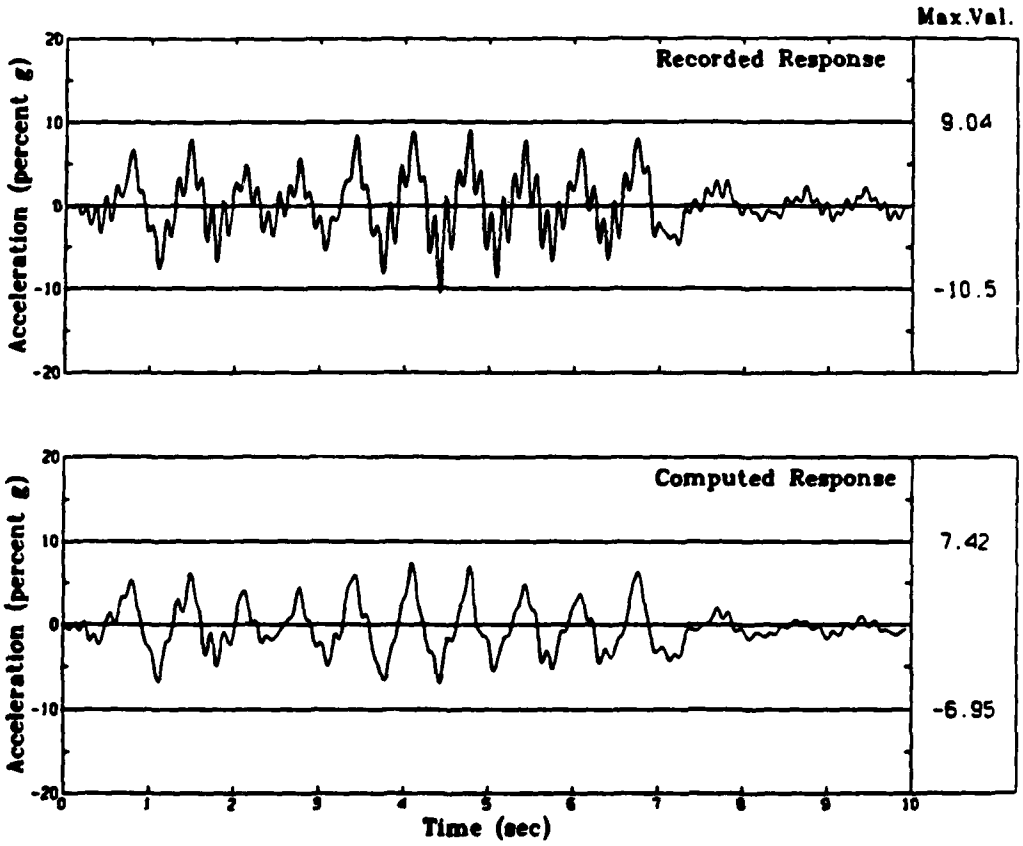

FIG. 21. Computed and measured accelerations at the location of ACC 3457 in test RSS110.

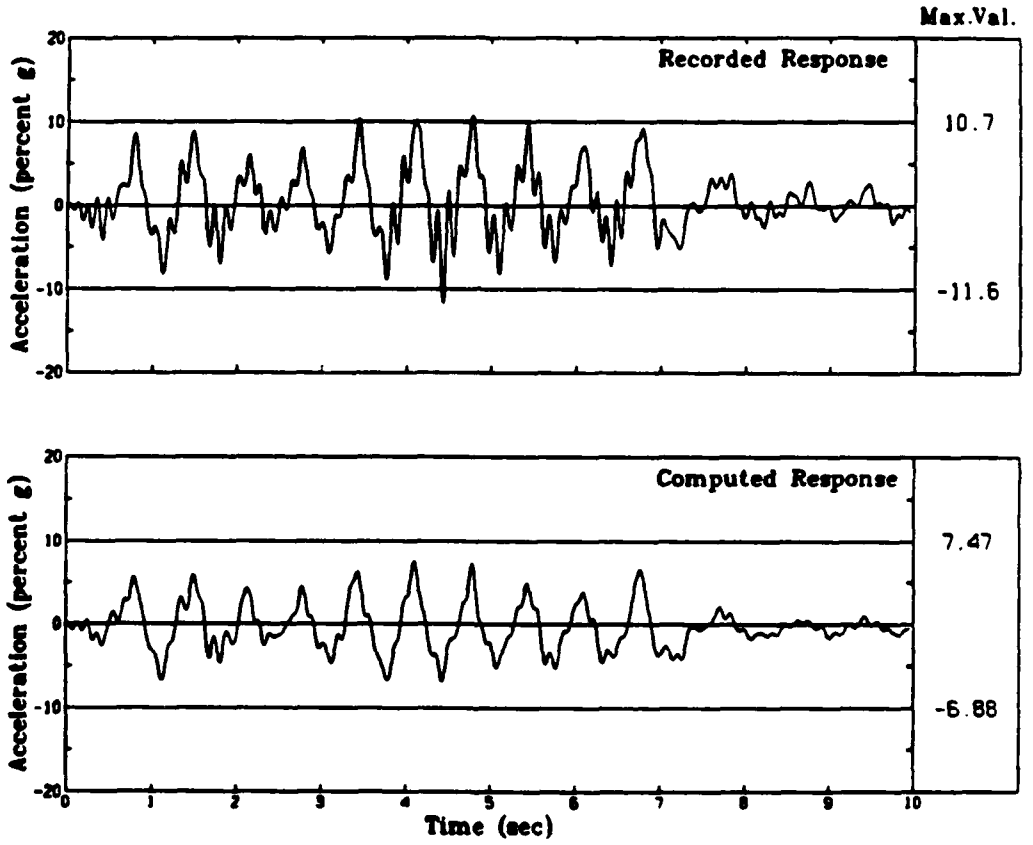

FIG. 22. Computed and measured accelerations at the location of ACC 1225 in test RSS110.

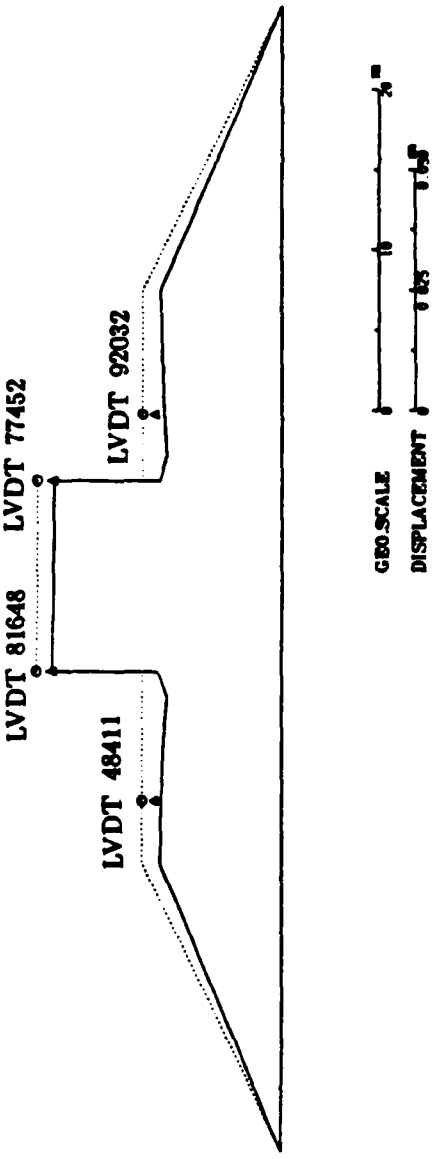

FIG. 23. Computed settlement pattern and measured settlements in test RSS110.

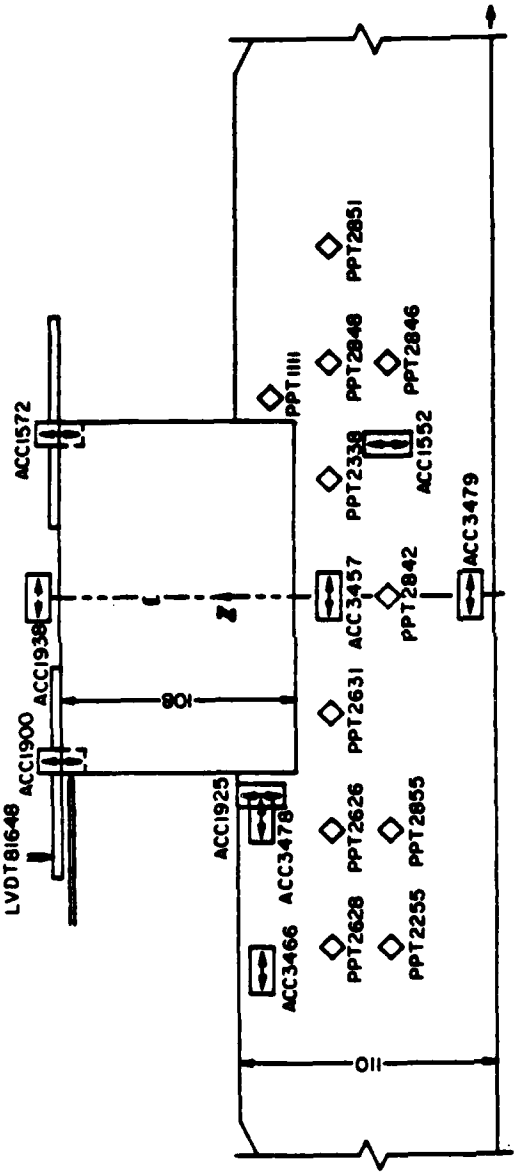

FIG. 24. Instrumentation layout in model test RSS111.

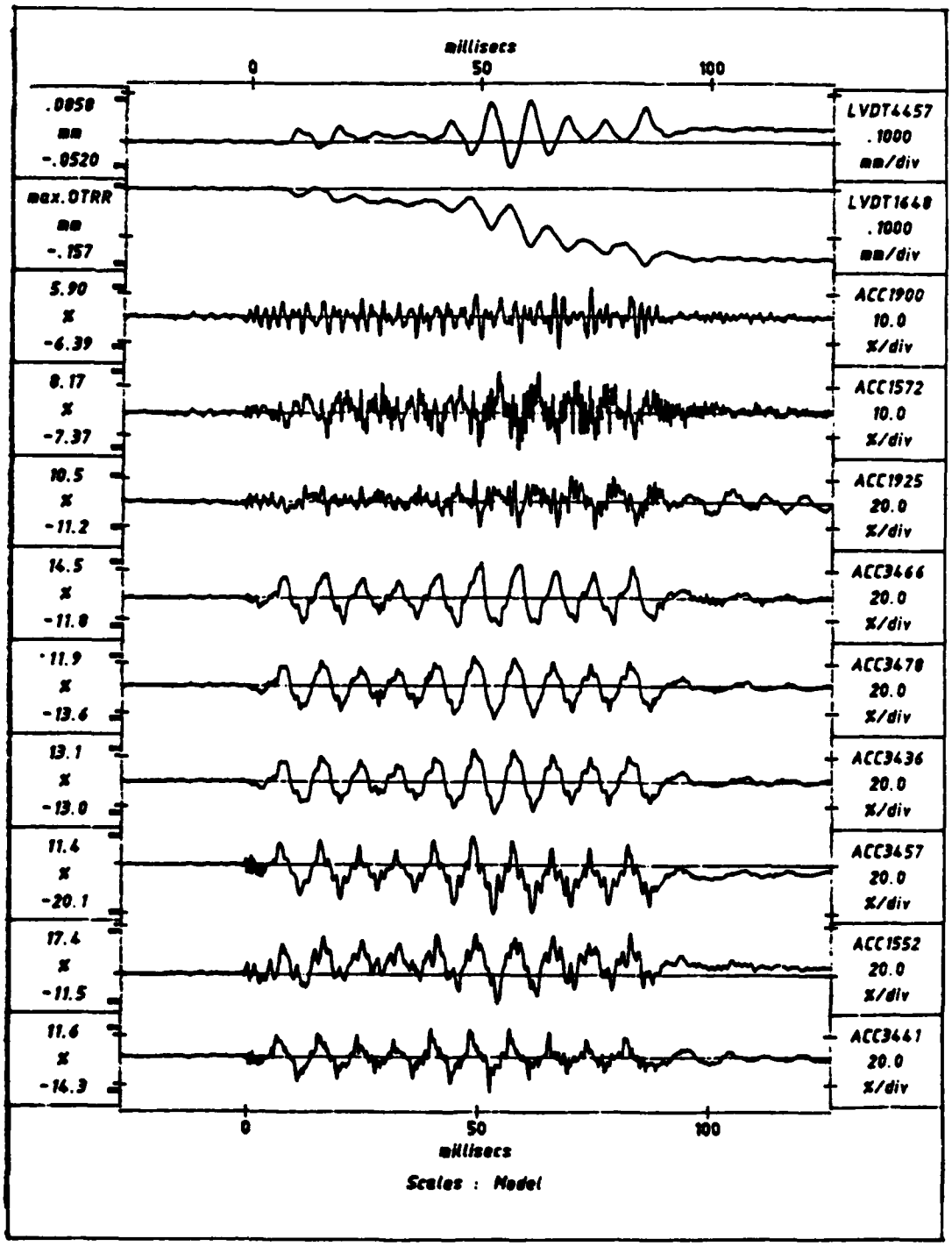

FIG. 25. Recorded data from test RSS111.

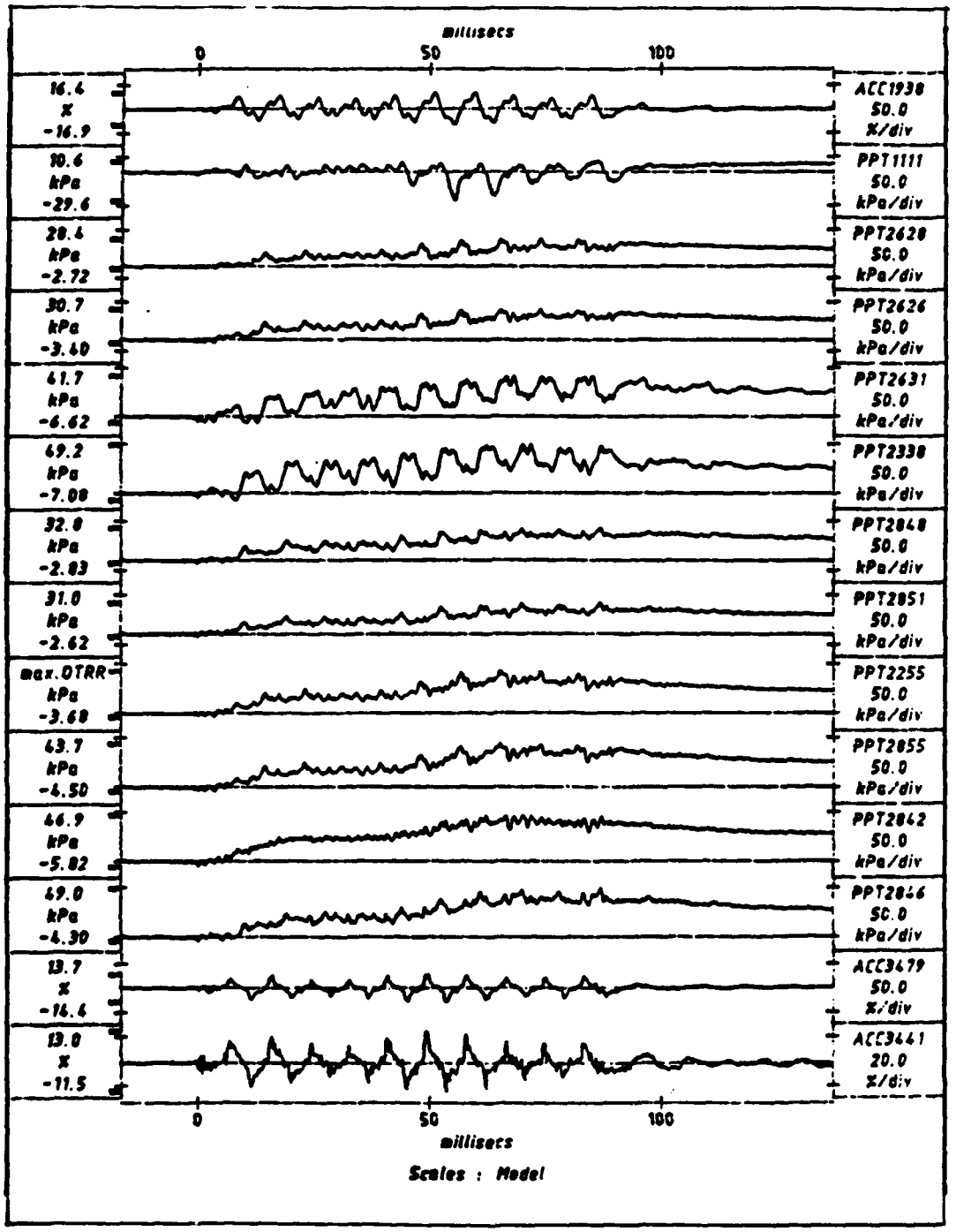

FIG. 26. Recorded data from test RSS111.

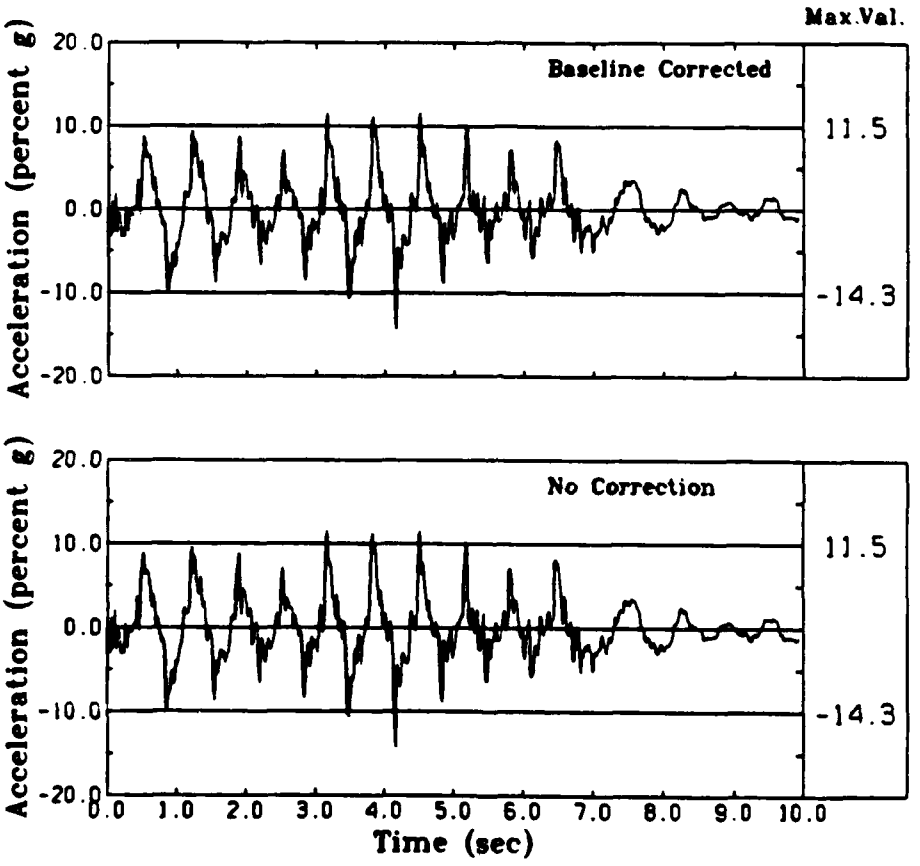

FIG. 27. Input motion for test RSS111.

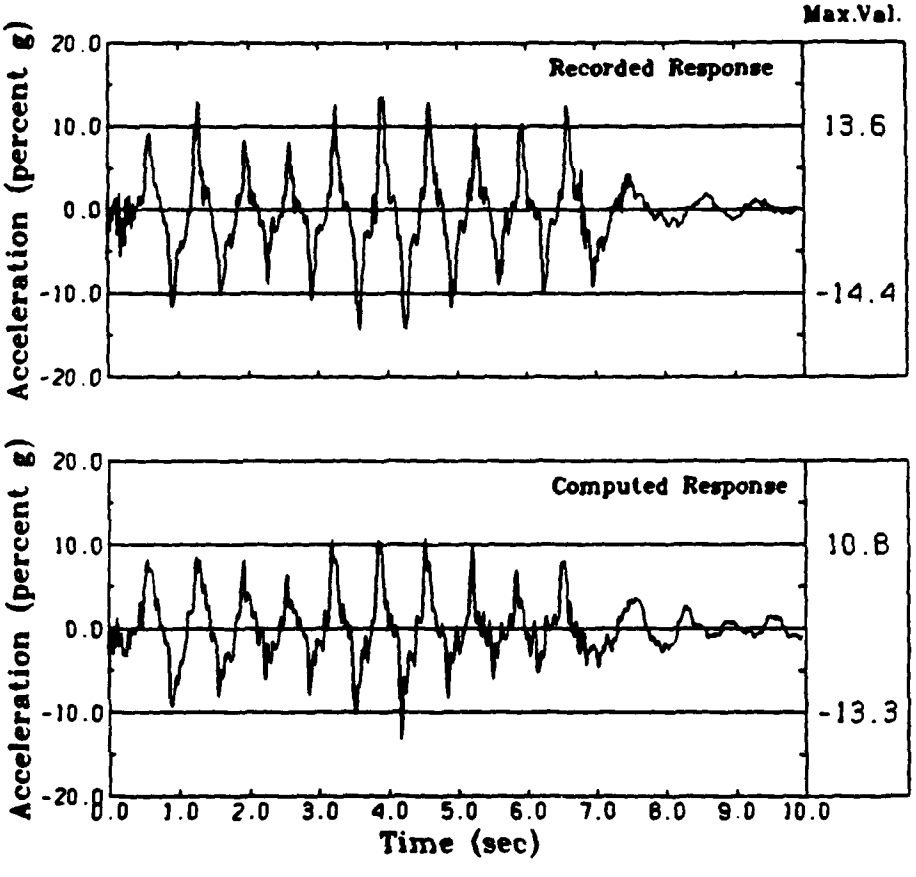

FIG. 28. Computed and measured accelerations at the location of ACC 3479 in test RSS111.

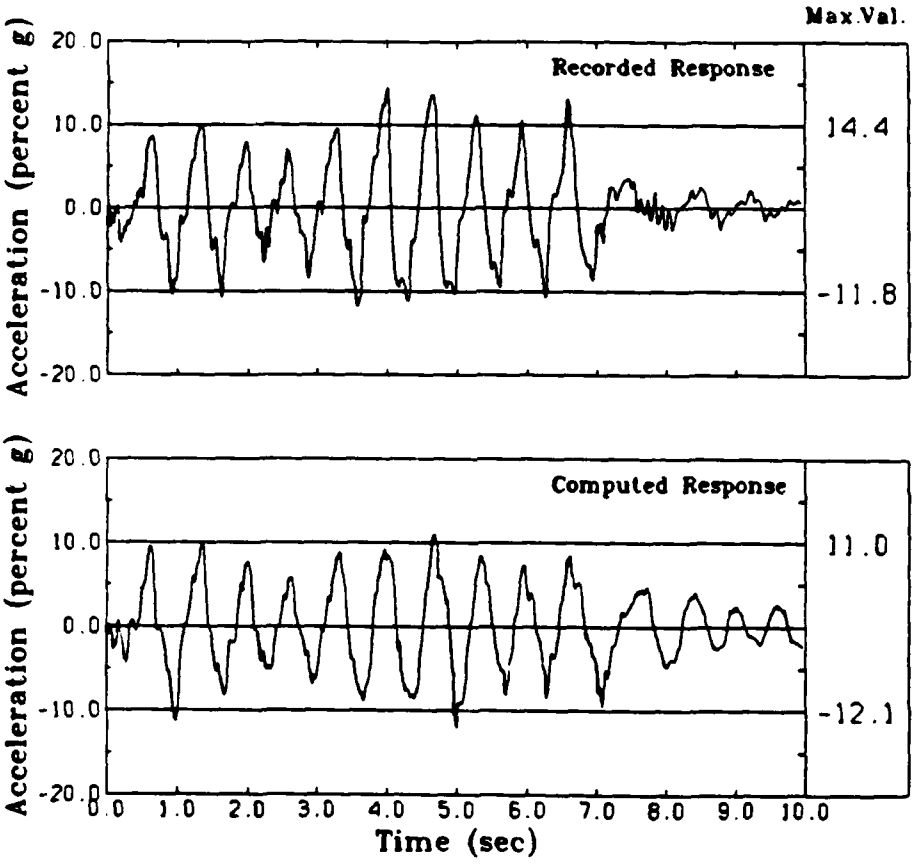

FIG. 29. Computed and measured accelerations at the location of ACC 3466 in test RSS111.

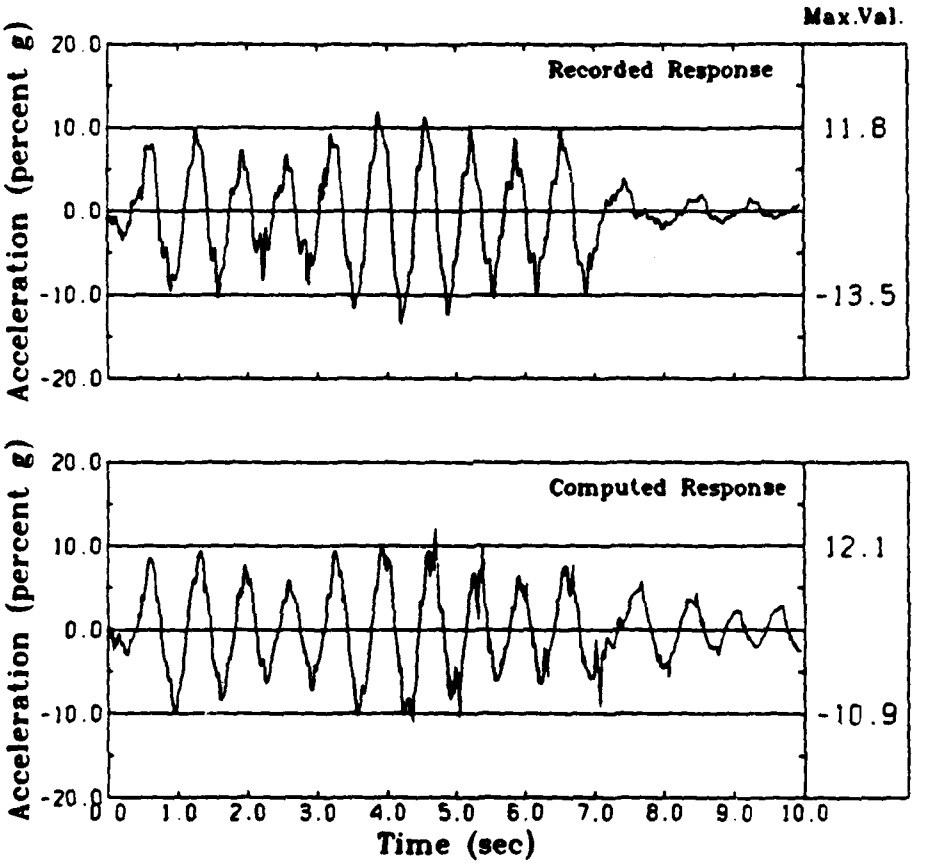

FIG. 30. Computed and measured accelerations at the location of ACC 3478 in test RSS111.

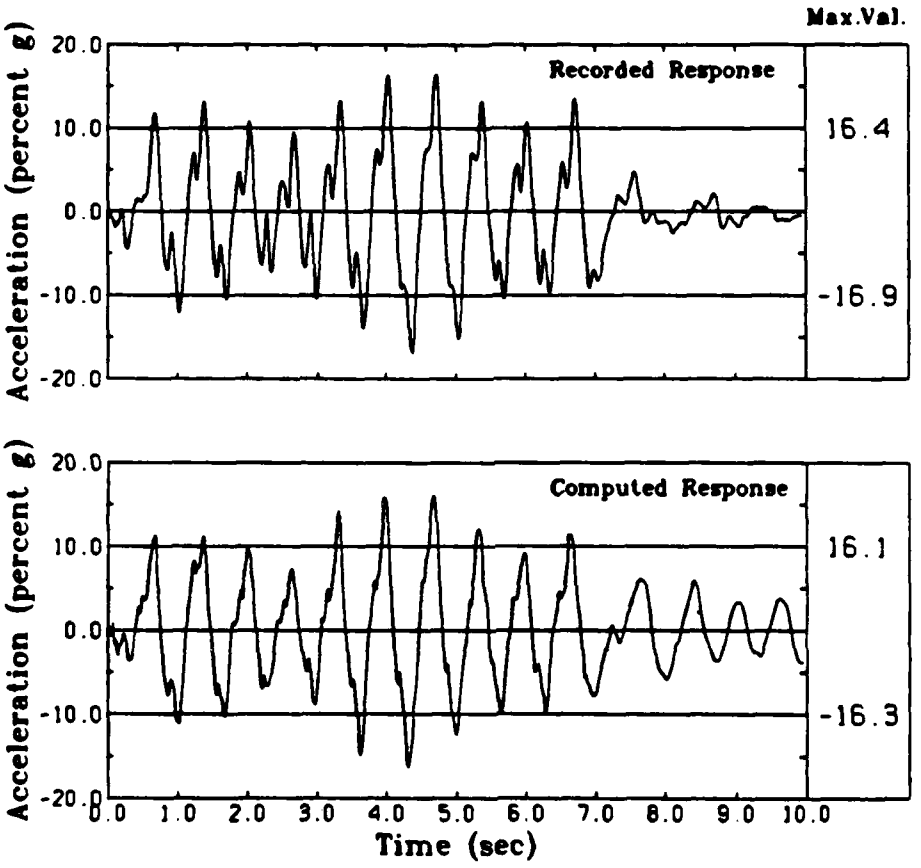

FIG. 31. Computed and measured accelerations at the location of ACC 1938 in test RSS111.

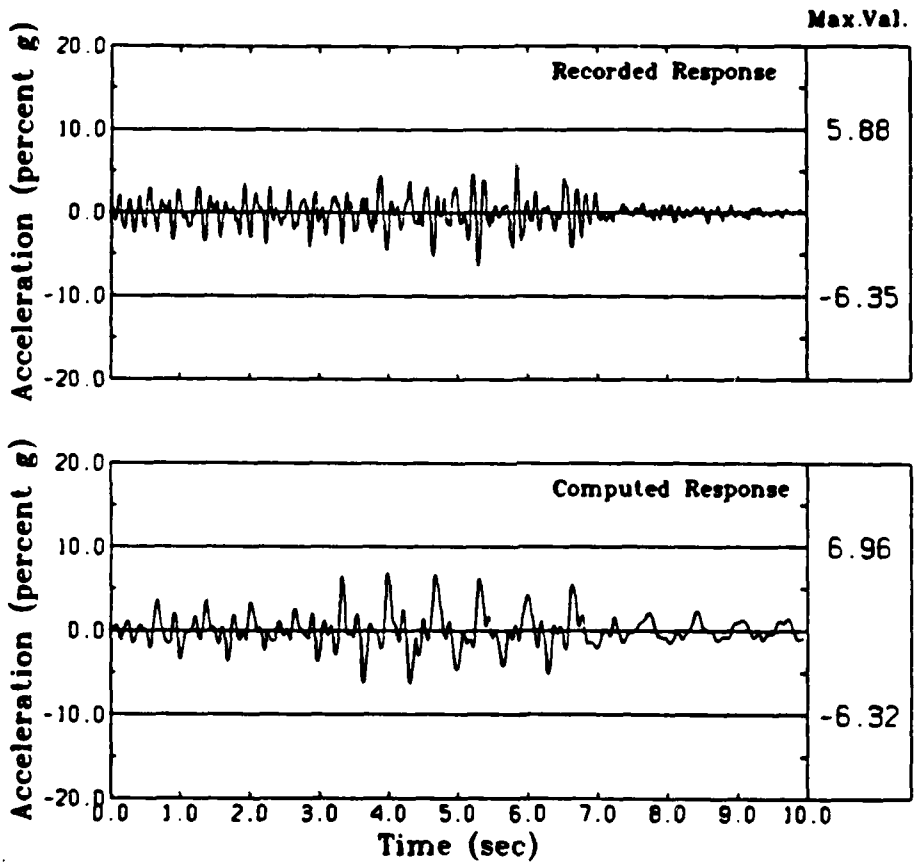

FIG. 32. Computed and measured accelerations at the location of ACC 1900 in test RSS111.

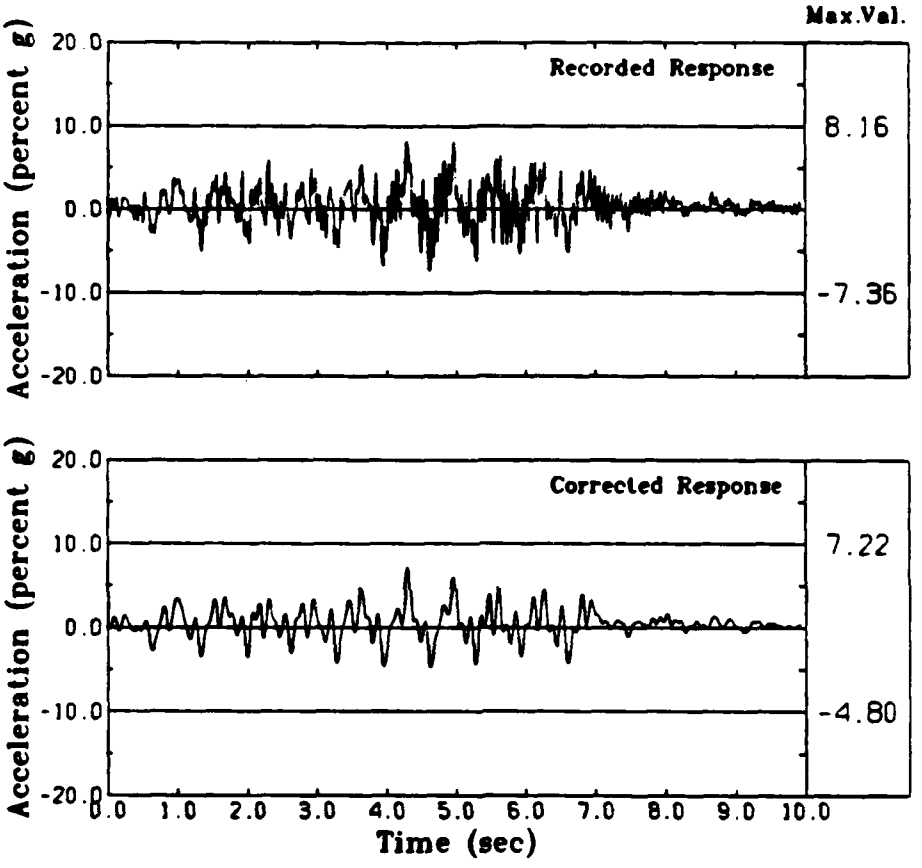

FIG. 33. Original and corrected accelerations at the location of ACC 1572 in test RSS111.

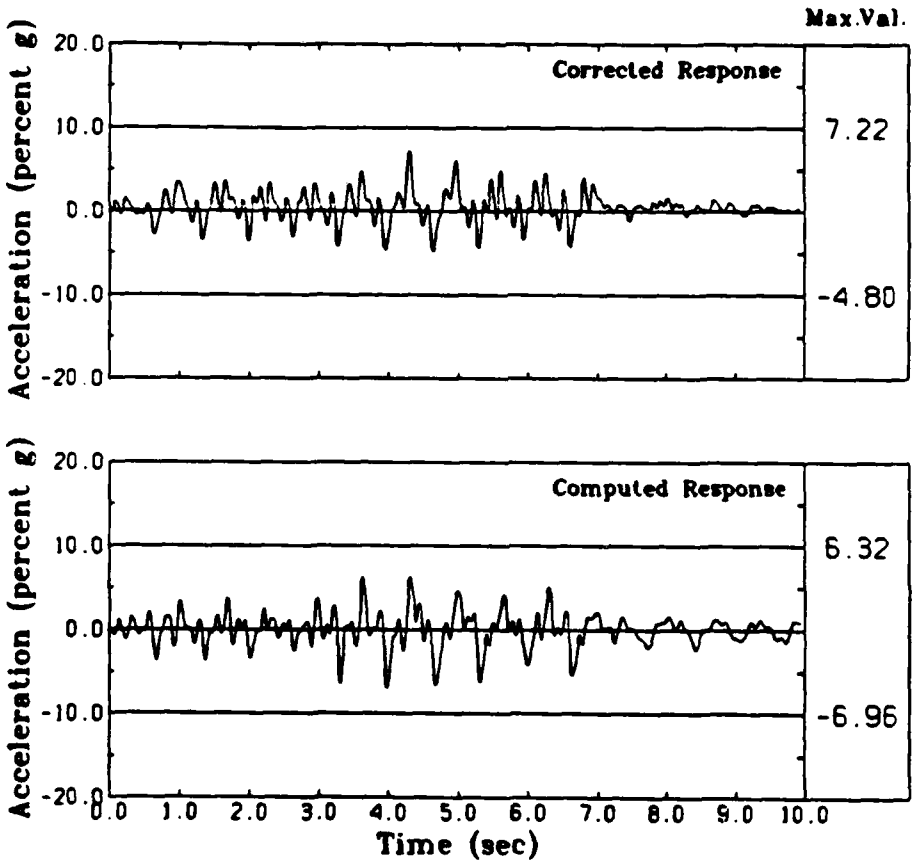

FIG. 34. Computed and corrected accelerations at the location of ACC 1572 in test RSS111.

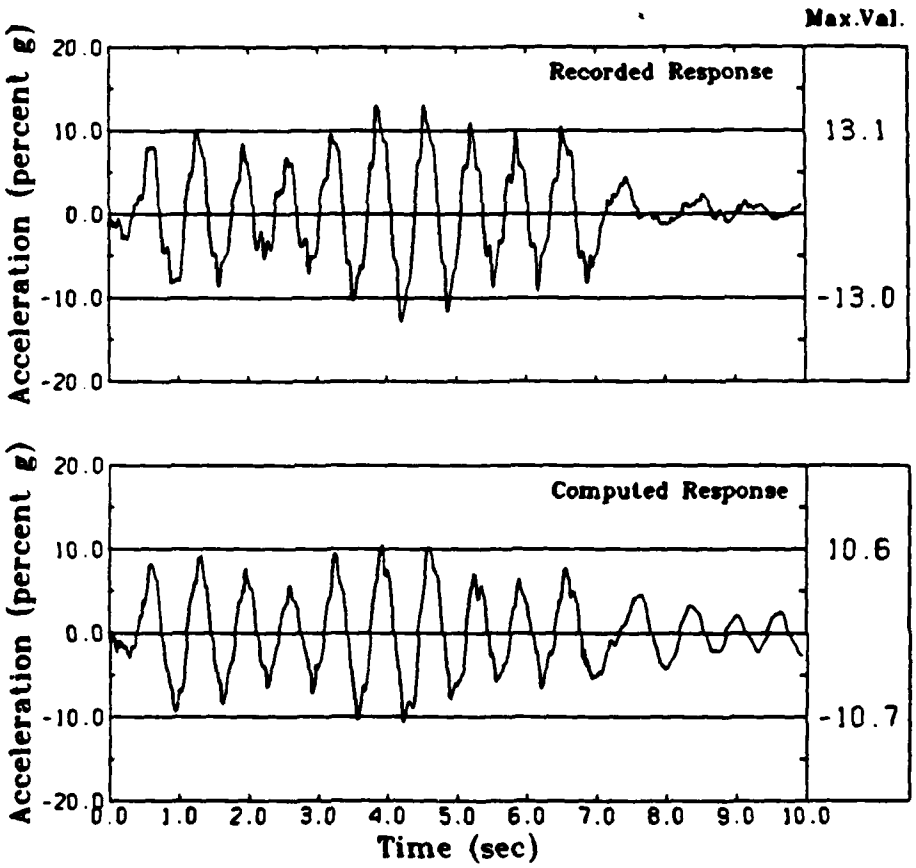

FIG. 35. Computed and measured accelerations at the location of ACC 3436 in test RSS111.

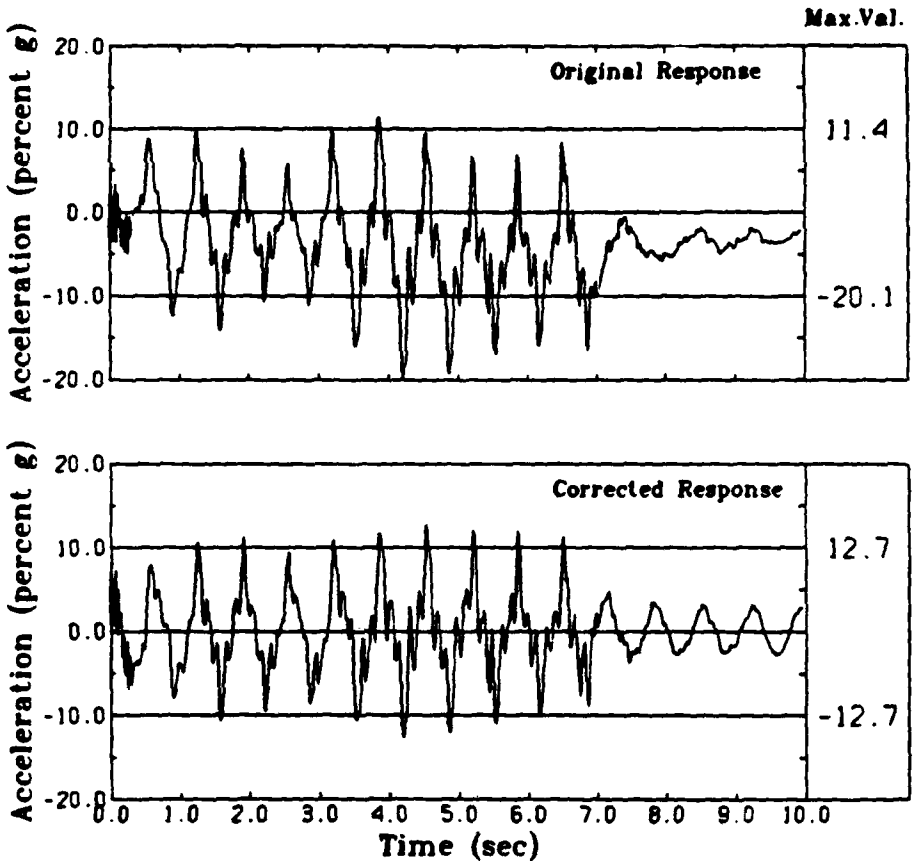

FIG. 36. Original and corrected accelerations at the location of ACC 3457 in test RSS111.

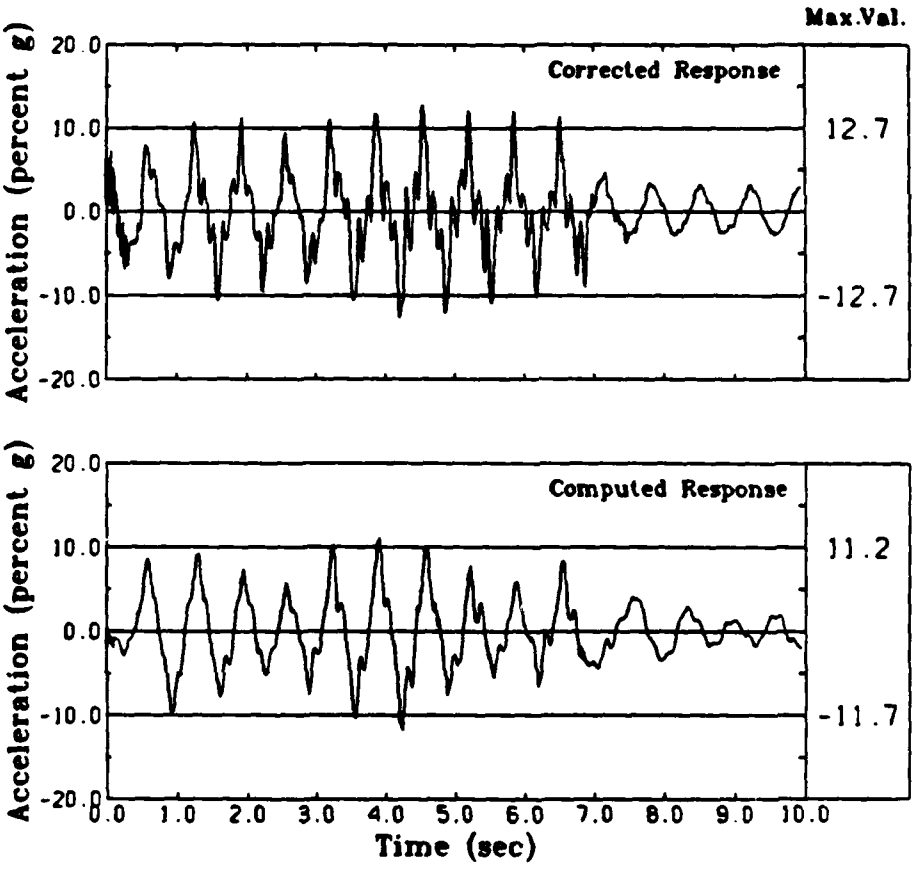

FIG. 37. Computed and corrected accelerations at the location of ACC 3457 in test RSS111.

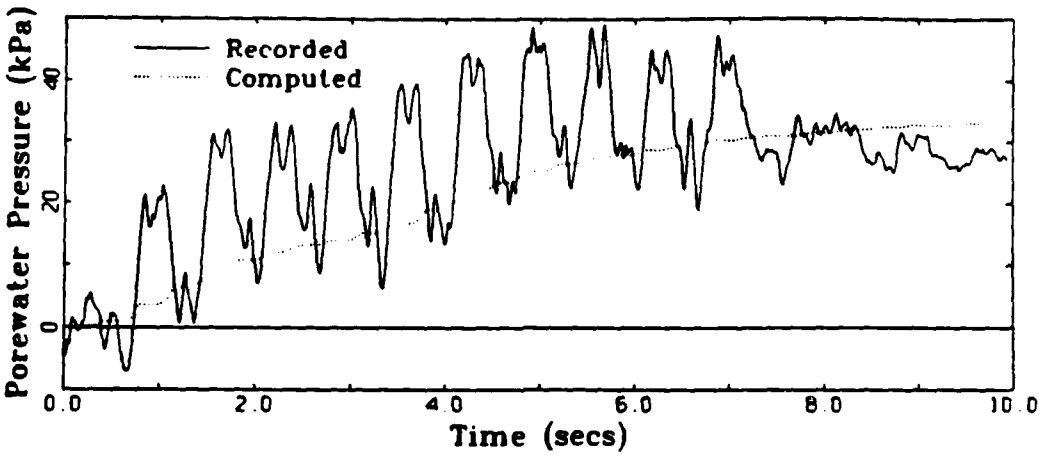

FIG. 38. Computed and measured porewater pressures at the location of PPT 2338 in test RSS111.

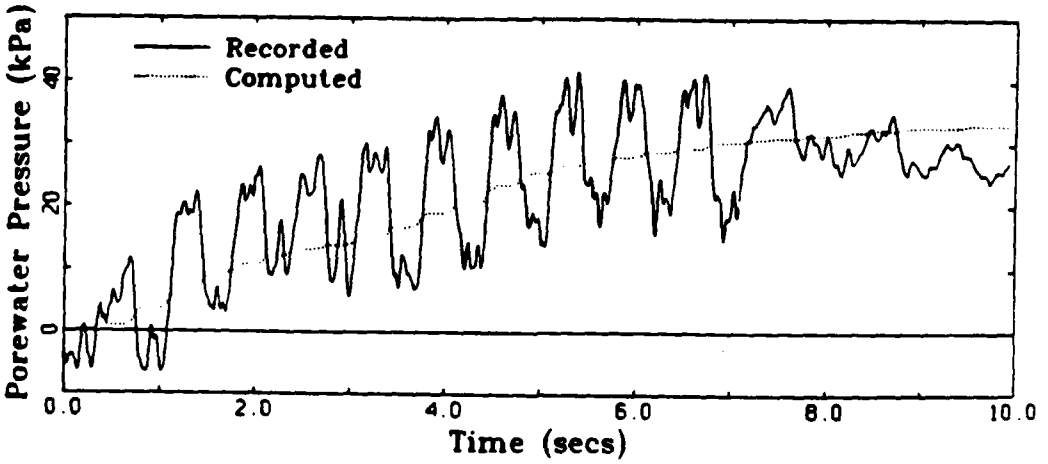

FIG. 39. Computed and measured porewater pressures at the location of PPT 2631 in test RSS111.

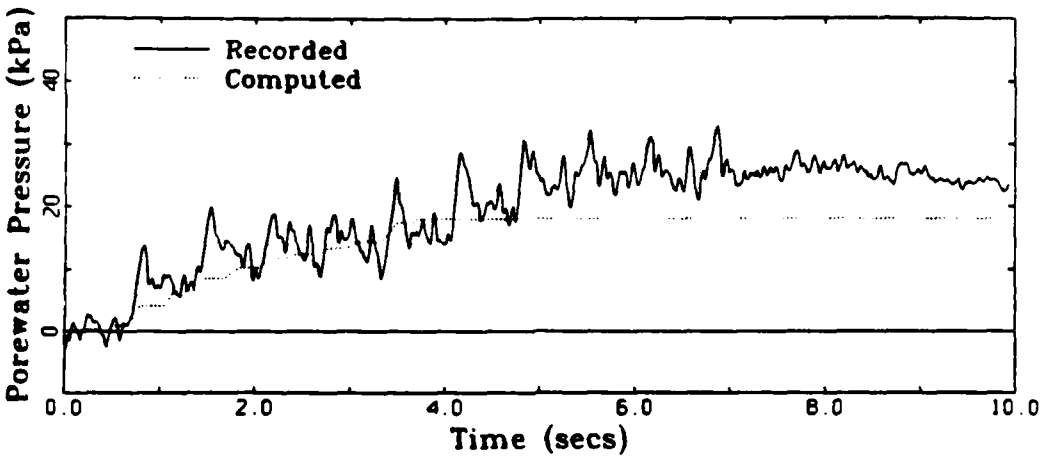

FIG. 40. Computed and measured porewater pressures at the location of PPT 2848 in test RSS111.

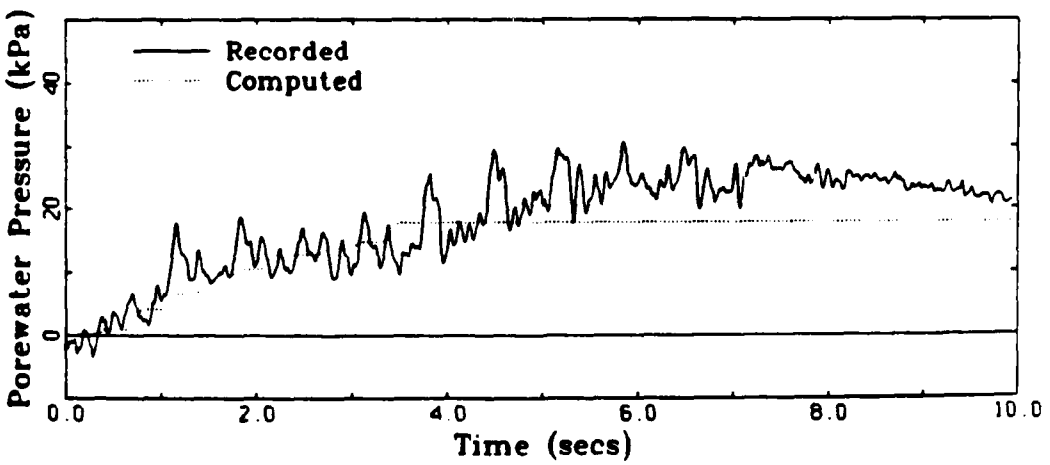

FIG. 41. Computed and measured porewater pressures at the location of PPT 2626 in test RSS111.

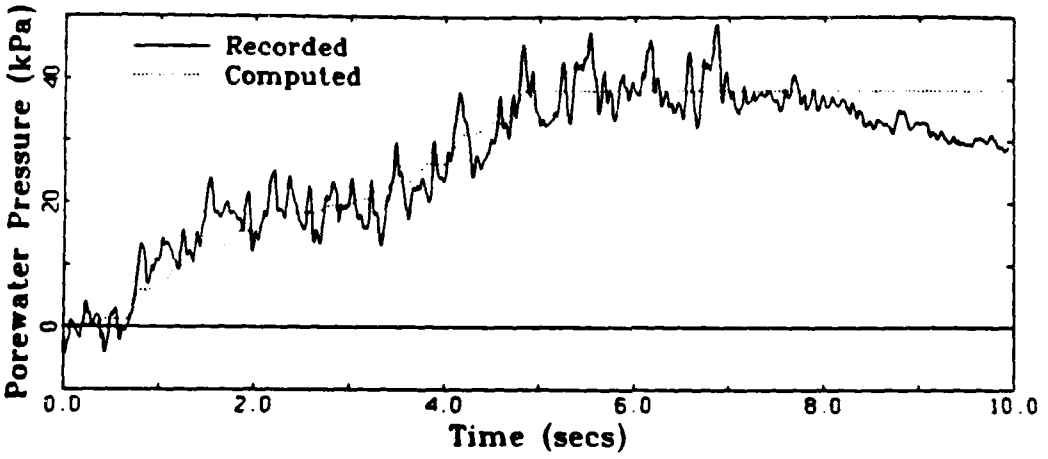

FIG. 42. Computed and measured porewater pressures at the location of PPT 2846 in test RSS111.

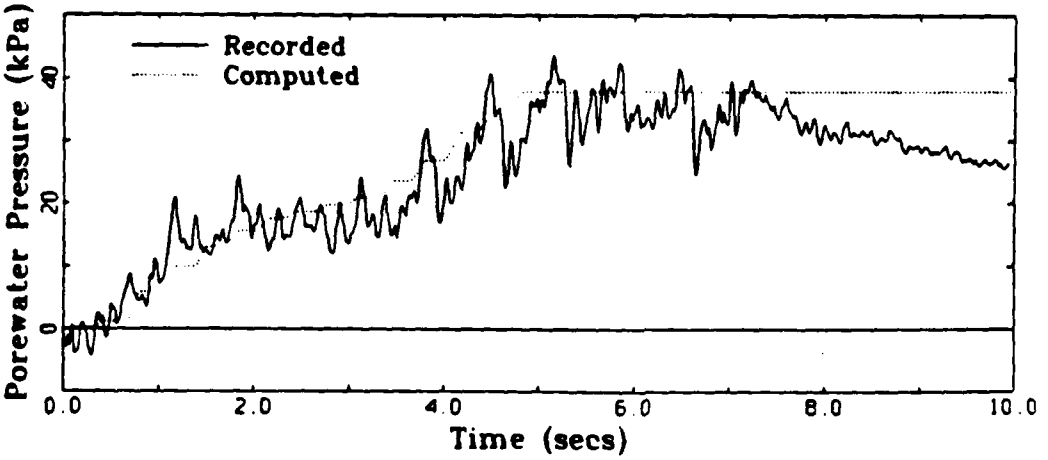

FIG. 43. Computed and measured porewater pressures at the location of PPT 2855 in test RSS111.

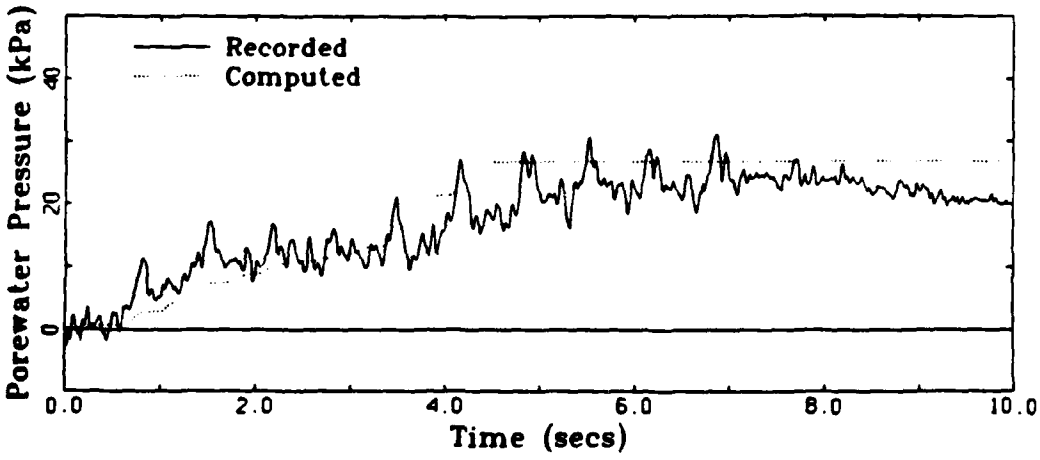

FIG. 44. Computed and measured porewater pressures at the location of PPT 2851 in test RSS111.

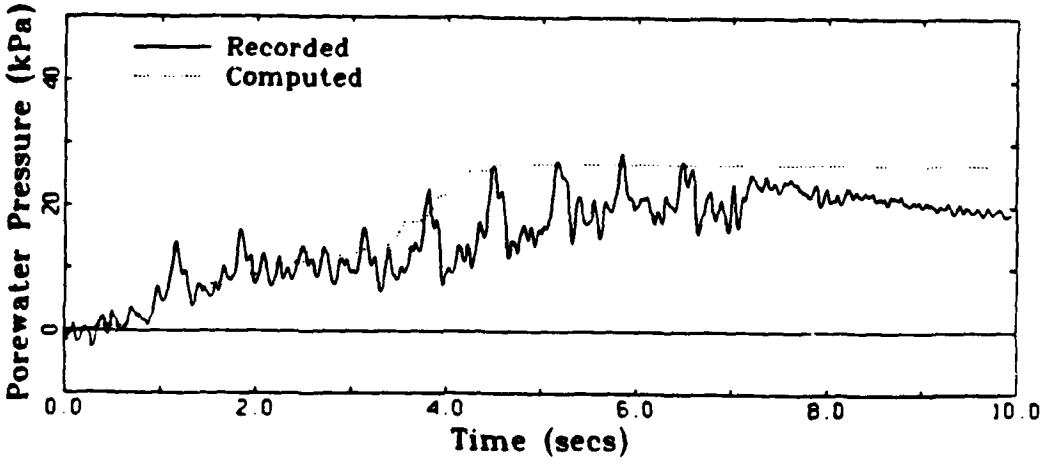

FIG. 45. Computed and measured porewater pressures at the location of PPT 2628 in test RSS111.

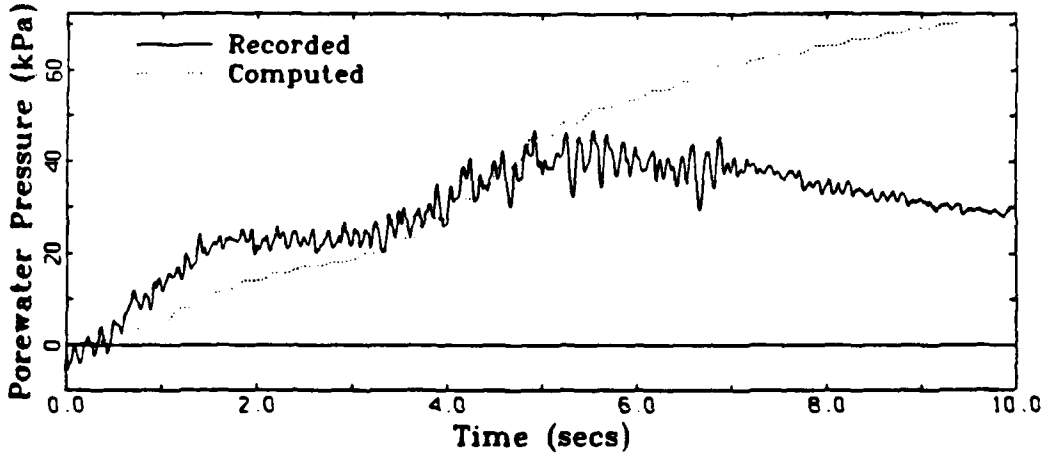

FIG. 46. Computed and measured porewater pressures at the location of PPT 2842 in test RSS111.

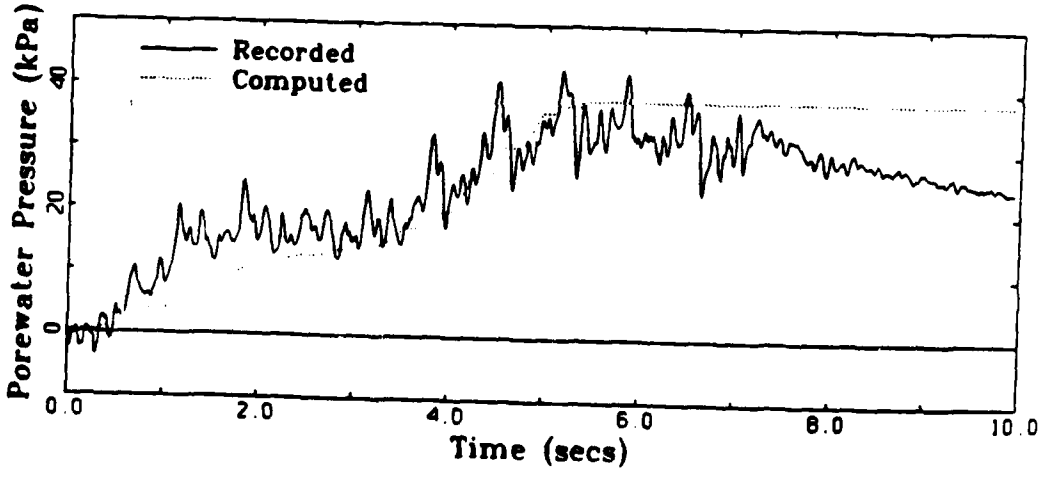

FIG. 47. Computed and measured porewater pressures at the location of PPT 2255 in test RSS111.

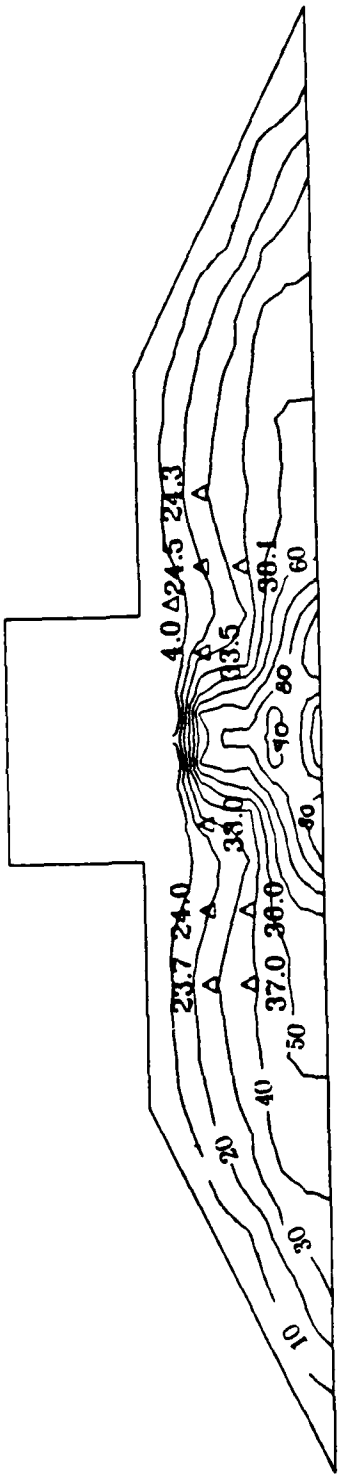

FIG. 48. Contours of computed peak residual porewater pressures.

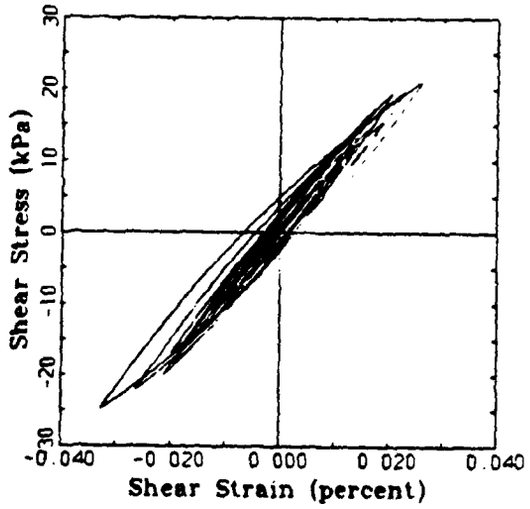

FIG. 49. Shear stress-strain response at the location of PPT 2338 in test RSS111.

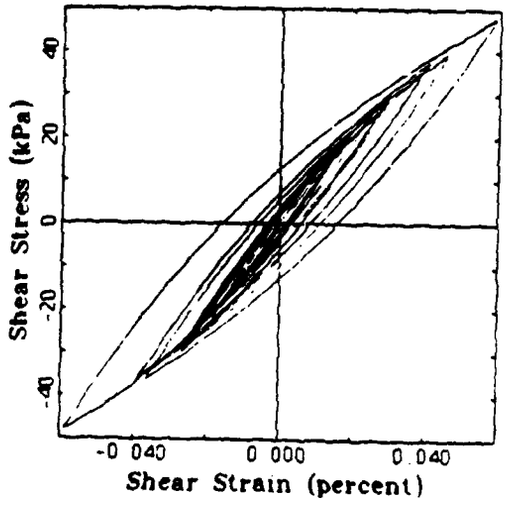

FIG. 50. Shear stress-strain response at the location of PPT 2842 in test RSS111.

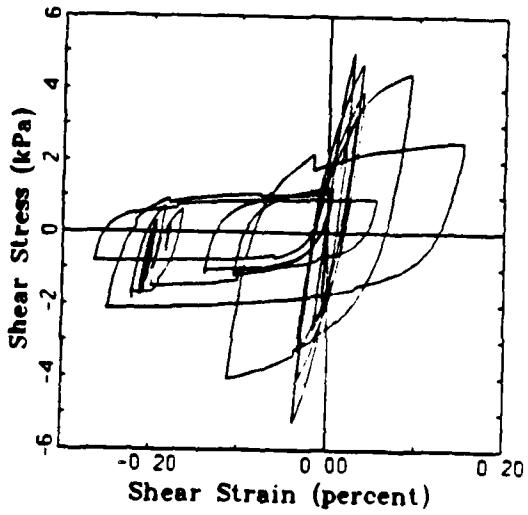

FIG. 51. Shear stress-strain response at the location of PPT 2851 in test RSS111.

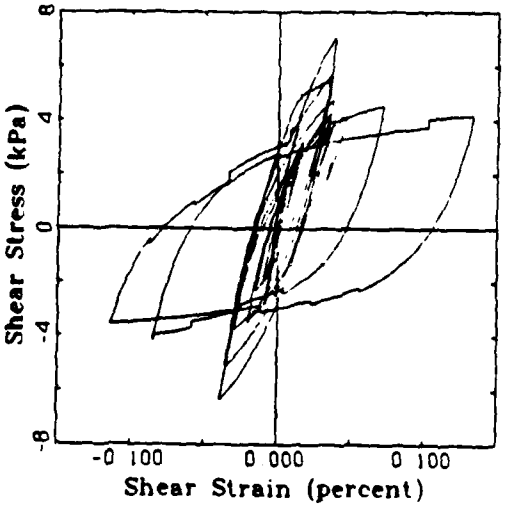

FIG. 52. Shear stress-strain response at the location of PPT 2848 in test RSS111.

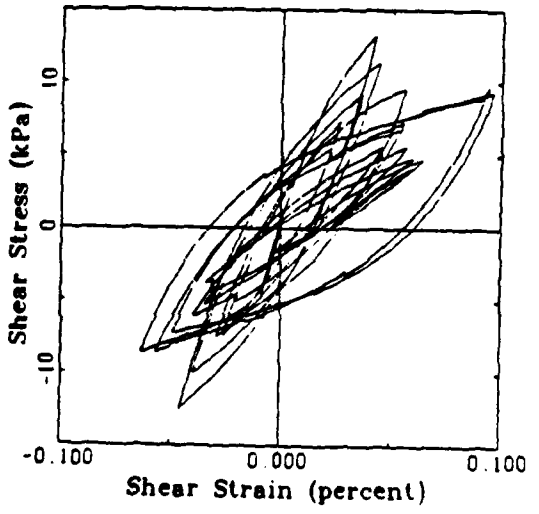

FIG. 53. Shear stress-strain response at the location of PPT 2846 in test RSS111.

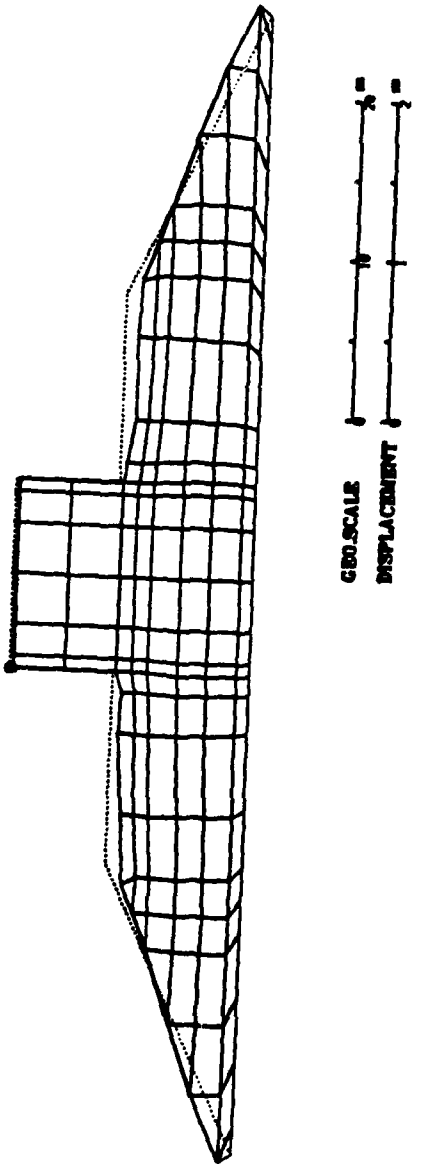

FIG. 54. Computed deformation pattern in test RSS111.